Computers and Geotechnics 173 (2024) 106477

Contents lists available at ScienceDirect

Computers and Geotechnics

journal homepage: www.elsevier.com/locate/compgeo

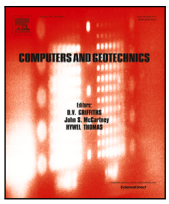

Research paper

Numerical investigation of artificial ground freezing–thawing processes in tunnel construction

R.J. Williams M. [a], M. Saberi [b], G. Meschke [a,*]

[a] Institute for Structural Mechanics, Ruhr University Bochum, Universitätsstr. 150, Bochum, 44801, Germany
[b] High Performance Computing, Ruhr University Bochum, Universitätsstr. 150, Bochum, 44801, Germany

ARTICLE INFO

Keywords:
Artificial ground freezing
Thawing
Tunneling
Finite element method

ABSTRACT

Artificial ground freezing is a frequently used method for temporary support of the soil in geotechnical interventions, such as tunneling. Besides the time required to form a supporting frozen soil structure during freezing, the prediction of temperature evolution during the thawing process and the final thawing time are also relevant, since settlements induced by thawing of the frozen soil can pose a risk to sensitive structures in urban tunneling. The freezing and thawing process of soils depends strongly on the unfrozen liquid content. The unfrozen liquid content during the freezing and thawing cycles is known to have a pronounced hysteresis response, whose effect on the temperature distribution and groundwater flow, especially at the structural level has not been extensively studied. In this work, we present a thermo-hydraulic finite element model for freezing soils and incorporate the hysteresis behavior of soil. We aim to investigate the suitability of the presented numerical model for tunnel construction on the one hand, and quantify the extent of the influence of the hysteresis response of the unfrozen liquid content at the structural level on the other. To this end, the model is first validated with the help of experimental data from a soil test subjected to a freezing–thawing cycle and subsequently used to analyze three problems of artificial ground freezing in tunnel construction during the freezing phase or freezing–thawing phases. The results show a good agreement with the experimental measurements. We show that the computational model is capable of providing accurate prognosis of the temperature profile as well as broader metrics such as the thickness and shape of the frozen body for tunneling applications under hydrostatic and seepage flow conditions. The hysteresis response is shown to have a significant influence on the coupled thermo-hydraulic process, with thawing times differing depending on whether hysteresis is considered. It is concluded, that the inclusion of the hysteresis response is crucial for obtaining an accurate representation of the freezing process.

1. Introduction

Artificial ground freezing (AGF) is a ground improvement technology employed during the construction of tunnels, mines, subsurface containment barriers and similar geotechnical projects with the primary purpose of controlling the groundwater flow and increasing the bearing capacity of the ground. The freezing of soil is a complex process, consisting of the interactions between phase transition in the pore liquid content, heat transfer affected by seepage flow and the mechanical deformation of the solid matrix. A number of mathematical formulations and numerical multi-field models have been proposed for the description of the coupled thermo-hydro-mechanical processes. The Theory of Porous Media (TPM), describing individual phases and their interactions within porous media (see, *e.g.* de Boer (2000) or Ehlers (1989)) has been adopted as the basis for several mathematical models for porous materials exposed to freezing see, e.g. Mikkola and Hartikainen (2002), Kruschwitz and Bluhm (2005) and Bluhm and Ricken (2007). A model based on thermo-poro-elasticity for water-infiltrated materials under freezing conditions, specifying the multi-scale physics of confined crystallization of ice, was presented in Coussy (2005).

A number of computational models have been developed for the numerical simulation of frozen porous materials. Examples of these computational models are the following: A thermo-hydro-mechanical finite element model with a critical-state elastoplastic soil formulation was presented in Nishimura et al. (2009) to study pipeline heave in soils, and a three-phase thermo-hydro-mechanical model based on the melting dynamics theory and thermo-poro-elasticity was presented in Zhou and Meschke (2013), where the undrained volumetric deformation during freezing of cement mortar was modeled. A three-phase

* Corresponding author.
E-mail address: guenther.meschke@rub.de (G. Meschke).

https://doi.org/10.1016/j.compgeo.2024.106477

Available online 13 June 2024
0266-352X/© 2024 The Author(s). Published by Elsevier Ltd. This is an open access article under the CC BY license (http://creativecommons.org/licenses/by/4.0/).

thermo-hydro-mechanical for multiphase freezing–thawing porous media in the finite deformation range was proposed by Na and Sun (2017), where the shear band formation in frozen soil was modeled. A three-phase thermo-hydraulic finite element model for freezing porous media was presented in Saberi et al. (2021a) where the formation of a frozen wall under seepage flow was modeled.

In the context of tunnel construction, artificial ground freezing methods are used to improve excavation conditions by creating a frozen area around the tunnel face (Jessberger, 1980; Hass et al., 1994; Hass and Schaefers, 2006). While abundant experimental and numerical studies have been dedicated to ground freezing in tunneling, the focus has often been tilted towards the freezing phase. The hydro-thermal interaction of soil freezing under different seepage velocities was experimentally investigated in a parametric study in Sres (2009). The sequential freezing of soil during the construction of a twin tunnel was experimentally studied in Cai et al. (2019), where the relevant monitoring data points of the temperature evolution during the freezing phase were provided. On the numerical side, a thermo-hydraulic finite difference numerical model was used to optimize the pipe arrangement with the goal of reducing energy consumption during the freezing phase in Baier (2008). A similar study was conducted in Marwan et al. (2016) using a thermo-hydraulic finite element model in conjunction with ant colony optimization to enhance the pipe distribution in order to reduce the time for the formation of the frozen body. The potential of numerical simulations in practical tunneling problems was studied in Pimentel et al. (2012a), where a thermo-hydraulic finite element model was employed to numerically reanalyze three examples of artificial ground freezing in urban underground construction projects. The feasibility of horizontal ground-freezing in shield-driven tunneling was investigated numerically in Hu et al. (2017), where heat transfer in the cup-shaped frozen soil wall was studied using a finite element model. Although such studies have provided insight into the freezing phase of ground freezing in tunneling applications, less attention has been paid to the thawing process. Recently, the temperature evolution of ground freezing and natural thawing of a frozen wall was studied using a model test in Cai et al. (2023). Similarly, the natural thawing of the horizontal ground-freezing method for soil reinforcement in shield-driven tunneling was simulated by means of a thermal finite element model in Fu et al. (2020).

It has been experimentally shown that the unfrozen water content in the soil during the freeze-thaw cycle exhibits hysteresis behavior, see Williams (1964), Koopmans and Miller (1966), Tian et al. (2014) and Vu et al. (2022). In particular, the experiments conducted in Tian et al. (2014) and Vu et al. (2022) show, that the freeze-thaw hysteresis is more pronounced for fine grain soils than for coarse grain soils and in case of mixed coarse-fine grain soils with a substantial portion of fine content. The freeze-thaw hysteresis has been attributed to capillary effects, pore blocking, metastable nucleation, electrolyte effects, etc., see Koopmans and Miller (1966), Spaans and Baker (1996) and Bittelli et al. (2003) for an extensive discussion of the physics of freeze-thaw hysteresis. According to literature models for the unfrozen water content of soils during the freezing processes were proposed, where hysteresis is not considered, e.g, see Anderson and Tice (1972), Zhang et al. (2017), Michalowsld (1993), McKenzie et al. (2007) and Kozlowski (2007). A comparison between the latter mentioned models and measurements was conducted by Lu et al. (2019). An investigation of suitable hysteresis models was performed by Zhou et al. (2019), and it was concluded that the models describing liquid water in unsaturated soil can be applied to describe unfrozen water in frozen soil using the same mathematical structure. A hysteresis model for the freezing and thawing processes in porous media was proposed in Saberi et al. (2021a), Saberi et al. (2021b), which follows a similar mathematical structure to the Van Genuchten water retention curve used in unsaturated soil mechanics. It was shown using a thermo-hydraulic finite element analysis that the model is capable of capturing the hysteresis response of soil and other porous media during freezing and thawing cycles.

In this work, we aim to provide a broader view of the thermo-hydraulic interaction during the application of artificial ground freezing in tunnel construction on the one hand by considering both freezing and thawing phases as well as seepage flow. On the other hand, given the hysteresis behavior of soil during freeze-thaw cycles, we aim to quantify the extent of the influence of such mechanisms in tunneling projects. More precisely, the evolution of the unfrozen water content in a single freezing–thawing cycle and heat transport by means of ground waterflow are considered. To this end, we employ a multi-field thermo-hydraulic finite element model for the freezing and thawing of soil. The model is an extension of the computational model for soil freezing presented in Zhou and Meschke (2013), coupled with the hysteresis model proposed in Saberi et al. (2021a), Saberi et al. (2021b). The computational model is implemented into the object-oriented framework of Kratos Multiphysics (Dadvand et al., 2010).

The structure of the remainder of this work is as follows: First, the theoretical background for the computational modeling of the ground freezing–thawing process is presented in Section 2. Next, the computational model is validated in Section 3 by means of numerical re-analysis of an experimental study documented in Cai et al. (2023) concerned with the freezing and thawing cycle of a frozen wall. Subsequently, three numerical studies of ground freezing in tunneling are presented in Section 4. The first study, in Section 4.1, focuses on modeling the temperature profile during sequential artificial ground freezing in the twin tunnel construction in Cai et al. (2019). The second example, presented in Section 4.2, investigates the thermo-hydraulic interaction of the artificial ground freezing process under seepage flow during the twin tunnel construction (Pimentel et al., 2012a). The final example focuses on the thawing process of the cup-shaped frozen zone in the horizontal freezing method in shield tunneling using the experimental data from Fu et al. (2020) and is presented in Section 4.3. Finally, conclusions are drawn in Section 5 regarding the prognosis of the freezing and thawing times of the soil, and the influence of the hysteresis behavior during the freezing and thawing cycle.

2. Numerical modeling of freezing and thawing of fully saturated soils

Freezing of pore water or thawing of pore crystal ice in soils results in changes in their material properties. These changes occur in the application AGF method in tunneling, which motivates the development of computational models for the numerical simulation of the freezing–thawing process in soils. The theoretical background of the freezing and thawing of soil is based on the theory of poromechanics of freezing material (Coussy, 2005) and the theory of premelting dynamics (Wettlaufer et al., 1996). The state of freezing and thawing of the soil is modeled as a three-phase porous material, consisting of solid particle (subscript S), liquid water (subscript L) and crystal ice (subscript C) as shown in Fig. 1. It is assumed that the pore volume is at all time fully-saturated – partly occupied by ice crystals (subscript $J = \mathrm{C}$) and partly occupied by the water remaining in liquid form (subscript $J = \mathrm{L}$). Denoting ϕ_J as partial porosity related to phase J, the porosity ϕ is written as

$$\phi = \phi_{\mathrm{L}} + \phi_{\mathrm{C}} \qquad \text{with } \phi_J = \chi_J \phi \tag{1}$$

where χ_J is the respective current saturation satisfying $\chi_{\mathrm{L}} + \chi_{\mathrm{C}} = 1$

2.1. Governing balance equations

The main governing equations for the freezing and thawing of fully saturated soil are the mass balance of liquid water and crystal ice, and the overall entropy balance, Eqs. (2) and (3) respectively, see Coussy (2005).

$$\frac{dm_L}{dt} + \frac{dm_C}{dt} + \nabla \cdot \boldsymbol{w}_{\mathrm{L}} = 0, \tag{2}$$

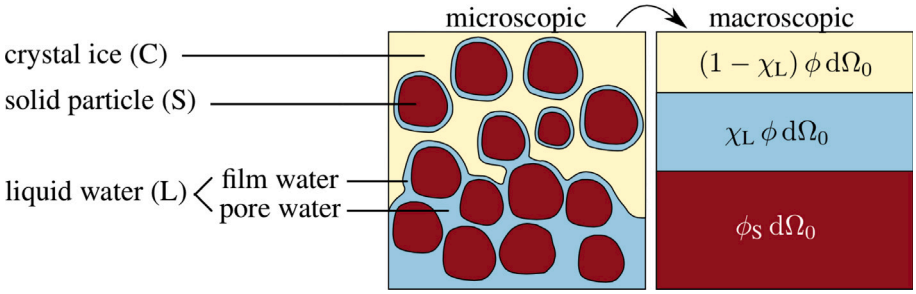

Fig. 1. Schematic illustration of Lagrangian porosity of the frozen fringe of a frost-susceptible soil (averaging principles are applied for transforming the microscopic model to macroscopic scale), from Zhou and Meschke (2013) and Marwan et al. (2016).

where $m_J = \rho_J \phi_J$ represents the current mass content related to phase J per unit volume, and $\boldsymbol{w}_{\mathrm{L}}$ stands for the liquid water flow relative to the soil skeleton.

$$T\left(\frac{dS}{dt} + \nabla \cdot (s_L \boldsymbol{w}_{\mathrm{L}})\right) + \nabla \cdot \boldsymbol{q} - \boldsymbol{\Phi}_M = 0, \tag{3}$$

with $S = S_{\mathrm{S}} + m_{\mathrm{L}} s_{\mathrm{L}} + m_{\mathrm{C}} s_{\mathrm{C}}$ as the overall density of entropy per unit of volume, S_{S} is the entropy of the solid matrix and s_J the specific entropy of the phase J, $\boldsymbol{q}$ is heat flow vector. Here, $\boldsymbol{\Phi}_M$ stands only for the mechanical dissipation associated with the viscous liquid flow through the porous volume. The format of the entropy balance Eq. (3) is convenient to use in weak forms for phase transition problems (see, e.g., Bonetti and Fremond (2003)).

2.2. Constitutive relations

2.2.1. Skeleton, water and ice entropies

The overall density of entropy per unit of volume, S can be expressed only in terms of the heat capacities of the skeleton c_{S}, liquid water c_{L} and ice crystal c_{C} by neglecting the contribution of the crystal ice pressure p_{C}, liquid water pressure p_{L} and the volumetric dilation of the skeleton ϵ. The entropy of the skeleton per unit volume is defined as

$$S_{\mathrm{S}} = S_{\mathrm{S0}} + \rho_{\mathrm{S}}(1-\phi_0) c_{\mathrm{S}} \frac{T - T_0}{T_0}, \tag{4}$$

where T_0 is the initial reference temperature. The specific entropy related to the ice or water phase J is defined as

$$s_J = s_{J0} + c_J \frac{T - T_0}{T_0}. \tag{5}$$

The freezing entropy S_f is the amount of entropy that has to be removed or added to the system to enable the phase change from liquid water to ice crystal or vice versa. The freezing entropy contribution appears during phase change due to the difference of the entropies of the crystal ice and liquid water, as follow:

$$s_{\mathrm{C}} - s_{\mathrm{L}} = (c_{\mathrm{C}} - c_{\mathrm{L}}) \frac{T - T_0}{T_0} - \frac{S_f}{\rho_{\mathrm{C0}}}, \tag{6}$$

where $S_f = \rho_{\mathrm{C0}}(s_{\mathrm{L0}} - s_{\mathrm{C0}}) > 0$ defines the freezing entropy per unit of volume with value $S_f = 1.2\mathrm{MPa/K}$, see Coussy (2005) and Birgersson et al. (2010). Moreover, S_f can be estimated analytically from the Clausius–Clapeyron relation by $S_f = \frac{L_f \rho_{\mathrm{L0}}}{T_f^{ref}}$, where $T_f^{ref} = 273.15\mathrm{K}$ is the freezing point of liquid water, ρ_{L0} is the initial density of the liquid water and $L_f = 334000\mathrm{J/kg}$ is the specific latent heat of fusion, see Black (1995).

2.2.2. Liquid saturation curves for freezing–thawing cycles

Non-hysteretic liquid saturation model: The relationship between the unfrozen liquid saturation and temperature without consideration for hysteresis is expressed via the following state equation:

$$\chi_L = \left(1 + \left(\frac{T_f - T}{\Delta T_{ch}}\right)^{\frac{1}{1-m}}\right)^{-m}, \tag{7}$$

where $\Delta T_{ch} = \frac{\mathcal{N}\gamma_{CL}}{S_f \gamma_{GL}}$ is the characteristic cooling temperature related to the most frequently encountered pore radius R_{ch}, and m is an index related to the pore radius distribution around R_{ch}, S_f denotes the freezing entropy per unit of volume .

Hysteretic liquid saturation model: The hysteresis behavior of the liquid saturation χ_L in freezing and thawing cycles is incorporated by the hysteresis model for unfrozen liquid content of Saberi et al. (2021a). The relationship between the liquid saturation and temperature is expressed via the following state equations for the main freezing and thawing branches as follows:

$$\chi_L = \begin{cases} \left(1 + \left|\alpha_f (T_f - T)\right|^{\frac{1}{1-m_f}}\right)^{-m_f} (\chi_{L,u} - \chi_{L,res}) + \chi_{L,res}, & \text{freezing branch,} \\ \left(1 + \left|\alpha_t (T_t - T)\right|^{\frac{1}{1-m_t}}\right)^{-m_t} (\chi_{L,u} - \chi_{L,res}) + \chi_{L,res}, & \text{thawing branch,} \end{cases} \tag{8}$$

where T_f and T_t denote the bulk freezing and thawing temperatures, respectively, $\chi_{L,u}$ and $\chi_{L,res}$ are the upper-bound and residual liquid contents, respectively, and α and m are shape parameters. The hysteresis model is illustrated in Fig. 2(a) and Fig. 2(b), evaluated for representative parameters. Upon monotonic freezing, when $\chi_{L,u} = 1$, $\chi_{L,res} = 0$, the parameter $\alpha_f = 1/\Delta T_{ch}$ can be interpreted as the inverse of the characteristic cooling temperature. The liquid saturation is then described based on the current state of the soil, i.e., either `freezing`, `thawing` or `thawed`:

$$\chi_L = \left(1 + \left|\alpha_f (T_f^* - T)\right|^{\frac{1}{1-m_f}}\right)^{-m_f} (\chi_L^* - \chi_{L,res}) + \chi_{L,res}, \tag{9}$$

if the soil is in the state of `freezing` or

$$\left(1 + \left|\alpha_t (T_t - T)\right|^{\frac{1}{1-m_t}}\right)^{-m_t} (\chi_{L,u} - \chi_L^*) + \chi_L^*, \tag{10}$$

if the soil is in the state of `thawing`. T_f^* and χ_L^* are history parameters that define the behavior of freezing and thawing scanning curves in the model. If the soil is fully thawed, $\chi_L = \chi_{L,u}$. We refer to Saberi et al. (2021a), Saberi et al. (2021b) for a detailed account of the hysteresis model and its integration into numerical codes.

2.2.3 Darcy's law

Adopting Darcy's law for describing the transport of the pore fluid, the Eulerian liquid flow can be expressed as

$$\boldsymbol{w}_L = \rho_{\mathrm{L0}} \boldsymbol{v}_{\mathrm{L}} = \rho_{\mathrm{L0}} \frac{\hat{\kappa}_0 \kappa_{rel}[\chi_L]}{\eta_0 \eta_{rel}[T]} (-\nabla p_L + \rho_{\mathrm{L0}} \boldsymbol{g}). \tag{11}$$

where $\boldsymbol{g}$ is the gravity force per unit volume, $g = \|\boldsymbol{g}\|$ is the euclidean norm of the gravity vector, $\hat{\kappa}_0$ is the intrinsic permeability, ρ_{L0} is the initial density of the liquid, κ_{rel} is the saturation dependent relative permeability as (Luckner et al., 1989)

$$\kappa_{rel}[\chi_L] = \sqrt{\chi_L} \left(1 - \left(1 - \chi_L^{\frac{1}{m}}\right)^m\right)^2. \tag{12}$$

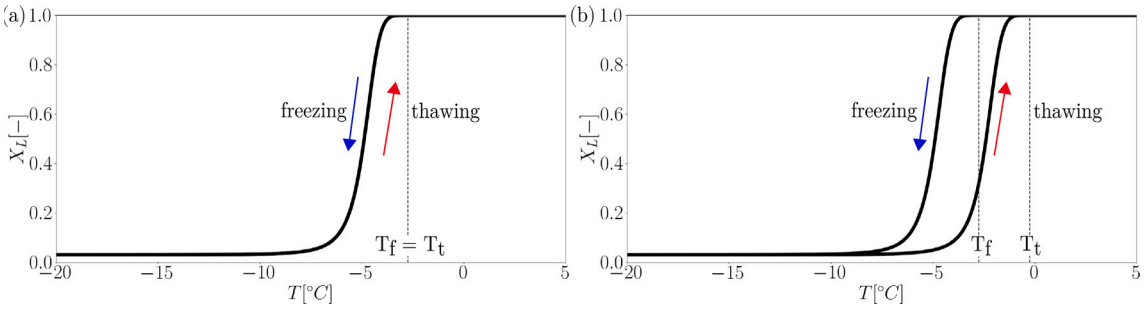

Fig. 2. Liquid saturation curve for a freezing–thawing cycle. (a) Non-hysteretic liquid saturation model with $\alpha_f = \alpha_t = 0.5$, $m_f = m_t = 0.82$, $T_f = T_t = =$ -2.75 °C, $\chi_{L,u} = 1.0$ and $\chi_{L,res} = 0.03$. (b) Hysteretic liquid saturation model with $\alpha_f = 0.5$, $m_f = 0.82$, T_f =-2.75 °C, $\alpha_t = 0.5$, $m_t = 0.82$, T_t = -0.25 °C, $\chi_{L,u} = 1.0$ and $\chi_{L,res} = 0.03$.

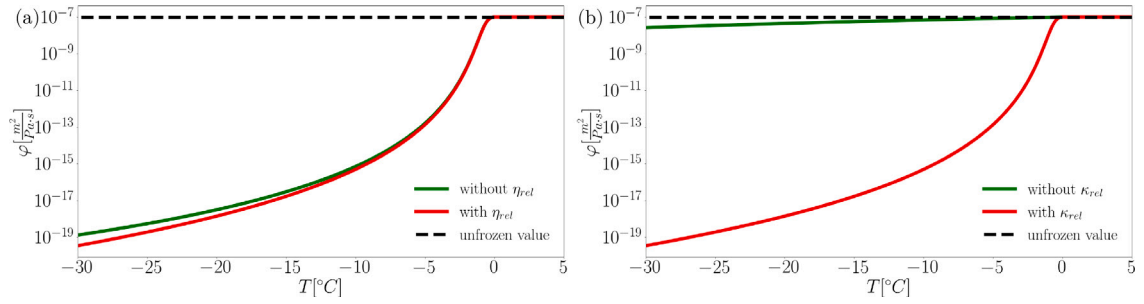

Fig. 3. Soil permeability like function φ upon freezing. (a) Influence of the empirical model for unfrozen super cooled water η_{rel}. (b) Influence of the relative permeability model κ_{rel}. The parameters used are $\hat{\kappa}_0 = 1E-10m2$, $\eta_0 = 1Pas$ and for the liquid saturation model $\alpha_f = 1.0$, $m_f = 0.7$, $T_f = 0.0$°C, $\chi_{L,u} = 1.0$, $\chi_{L,res} = 0$.

η_0 is the reference viscosity at $T = T_f$, the temperature depence of the viscosity of supercooled water is represented by η_{rel}, which is defined by the empirical relation (Grant, 2000)

$$\eta_{\text{rel}}[T] = 1.5963 \times 10^{-2} \times e^{\frac{509.53}{123.15 - (T_f - T)}}. \tag{13}$$

In contrast to the variation of relative permeability with temperature, which reproduces the waterproofing effect of ground freezing, the variation of liquid water viscosity with temperature has minimal influence on the velocity of expelled water, as shown in Tounsi et al. (2019), Vitel et al. (2016). We study this by defining the function $\varphi = \frac{\hat{\kappa}_0\,\kappa_{rel}[\chi_L]}{\eta_0\,\eta_{rel}[T]}$ which represents the decrease of permeability upon freezing. The Fig. 3 shows the evolution of the function φ upon freezing under the influence of the viscosity of super cooled water Eq. (13) and the relative permeability model Eq. (12). The Eulerian liquid flow $\boldsymbol{w}_L$ can be expressed as in terms of the hydraulic conductivity or permeability κ by the use of the relation $\frac{\hat{\kappa}_0}{\eta_0} = \frac{\kappa_0}{\rho_{L0}\,g}$. Disregarding the effects of Eq. (13), the Eulerian liquid flow $\boldsymbol{w}_L$ is expressed as

$$\boldsymbol{w}_L = \frac{\kappa_0\,\kappa_{rel}[\chi_L]}{g}\,(-\nabla p_L + \rho_{L0}\,\boldsymbol{g}). \tag{14}$$

Furthermore, the mechanical dissipation caused by the viscous liquid flow can be expressed as see Coussy (2005),

$$\boldsymbol{\Phi}_M = \frac{\kappa_0\,\kappa_{rel}[\chi_L]}{\rho_{L0}\,g}\,(-\nabla p_L + \rho_{L0}\,\boldsymbol{g})\cdot(-\nabla p_L + \rho_{L0}\,\boldsymbol{g}). \tag{15}$$

2.2.4 Fourier's law

Adopting Fourier's law, the heat flux is connected to the temperature gradient via

$$\boldsymbol{q} = -\lambda_{tot}\,\nabla T, \tag{16}$$

$$\lambda_{tot} = \lambda_S^{1-\phi_o}\,\lambda_L^{\phi_o \chi_L}\,\lambda_c^{\phi_o(1-\chi_L)} \tag{17}$$

In the equation above, λ_{tot} stands for the overall thermal conductivity,where λ_S, λ_L and λ_C are thermal conductivities of solid particles, liquid water, and crystal ice, respectively, (Côté and Konrad, 2005).

2.3 Hydro-thermal finite element formulation

In the context of the multi-field finite element method formulation within the framework of the geometrically linear theory, the model for soil freezing and thawing is formulated as Initial Boundary Problem (IBVP) in the spatial domain Ω for the time period $[0, t]$. IBVP is formulated by transforming the balance equations to their variational form with the selected set of primary variables ($\boldsymbol{d} = \begin{bmatrix} p_{\text{L}} & T \end{bmatrix}^T$). The variational form is obtained by multiplication with the test functions $\boldsymbol{\delta d}$ and integrated over the domain Ω, which to the following weak forms

$$\begin{aligned}
\delta W^1 &= \int_{\Gamma_N^1} \delta p_{\text{L}}\, w^*\,\mathrm{d}A + \int_\Omega \delta p_{\text{L}} \left(\frac{\mathrm{d}\,m_{\text{L}}}{\mathrm{d}\,t} + \frac{\mathrm{d}\,m_{\text{C}}}{\mathrm{d}\,t}\right)\mathrm{d}V \\
&\quad - \int_\Omega \boldsymbol{\nabla}\boldsymbol{\delta p}_{\text{L}} \cdot \boldsymbol{w}_{\text{L}}\,\mathrm{d}V = 0, \\
\delta W^2 &= \int_{\Gamma_N^{2'}} \delta T\, q^*\,\mathrm{d}A + \int_\Omega \delta T\, T \left(\frac{\mathrm{d}\,S_{\text{S}}}{\mathrm{d}\,t} + \frac{\mathrm{d}\,m_{\text{C}}}{\mathrm{d}\,t}\,(s_{\text{C}} - s_{\text{L}})\right. \\
&\quad \left. + m_{\text{L}}\,\frac{\mathrm{d}\,s_{\text{L}}}{\mathrm{d}\,t} + m_{\text{C}}\,\frac{\mathrm{d}\,s_{\text{C}}}{\mathrm{d}\,t}\right)\mathrm{d}V \\
&\quad + \int_\Omega \delta T\, T\, \boldsymbol{\nabla} s_{\text{L}} \cdot \boldsymbol{w}_{\text{L}}\,\mathrm{d}V - \int_\Omega \boldsymbol{\nabla}\boldsymbol{\delta T} \cdot \boldsymbol{q}\,\mathrm{d}V - \int_\Omega \delta T\, \boldsymbol{\Phi}_M\,\mathrm{d}V = 0,
\end{aligned} \tag{18}$$

supplemented by the following boundary and initial conditions

Dirichlet boundary	Neumann boundary	Initial conditions
$\forall\, \boldsymbol{x} \in \Gamma_D^1 : \quad p_{\text{L}} = p_{\text{L}}^*,$	$\forall\, \boldsymbol{x} \in \Gamma_N^1 : \quad \boldsymbol{w}_{\text{L}} \cdot \boldsymbol{n} = w^*,$	$\forall\, \boldsymbol{x} \in \Omega : \quad p_{\text{L}} = p_{\text{L0}},$
$\forall\, \boldsymbol{x} \in \Gamma_D^2 : \quad T = T^*,$	$\forall\, \boldsymbol{x} \in \Gamma_N^2 : \quad \boldsymbol{q} \cdot \boldsymbol{n} = q^*,$	$\forall\, \boldsymbol{x} \in \Omega : \quad T = T_0.$

For the spatial discretization, the primary variables $\boldsymbol{d}$ are approximated using linear shape functions. The temporal discretization is formulated using the generalized-α time integration scheme. In this scheme, the variational forms are evaluated at the generalized midpoint of each time step $t_{n+1-\alpha}$ as $t_{n+1-\alpha} = \alpha t_n + (1-\alpha)t_{n+1}$, see Kuhl and Crisfield (1999). The integration parameters are chosen to assure unconditional stability and second order accuracy without any additional numerical dissipation, $\alpha_m = \alpha_f = \frac{1}{2}$, $\beta = \frac{1}{4}$ and $\gamma = \frac{1}{2}$. Finally, the spatial

Table 1
Freeze-thaw numerical model: Material properties of unfrozen and frozen sand.

	Initial Density	Heat capacity	Thermal conductivity	Porosity	Freezing entropy
	ρ kg/m^3	c J/(kg K)	λ W/(m K)	ϕ –	S_f MPa/K
Sand	2650	740	7.694	0.42	
Water	1000	4200	0.611	–	
Ice	913	1900	2.222	–	1.2

and temporal discretization of the weak forms result in a set of highly nonlinear algebraic equations.

This nonlinear system is linearized and solved iteratively by means of the Newton-Raphson scheme, leading to the update scheme

$$\boldsymbol{\Delta d}_{n+1}^{k+1} = \left((1-\alpha_f)\boldsymbol{K}^k + (1-\alpha_f)\frac{\lambda}{\beta \Delta t}\boldsymbol{D}^k\right)^{-1}_{n+1-\alpha}\left(\boldsymbol{R}_{ext} + \boldsymbol{R}_{int}^k\right)_{n+1-\alpha} \tag{19}$$

and

$$\boldsymbol{d}_{n+1}^{k+1} = \boldsymbol{\Delta d}_{n+1}^{k+1} + \boldsymbol{d}_{n+1}^{k} \tag{20}$$

with

$$\boldsymbol{\Delta d} = \begin{bmatrix} \boldsymbol{\Delta} p_L \\ \boldsymbol{\Delta T} \end{bmatrix}, \ \boldsymbol{K} = \begin{bmatrix} \boldsymbol{K}_{pp} & \boldsymbol{K}_{pT} \\ \boldsymbol{K}_{Tp} & \boldsymbol{K}_{TT} \end{bmatrix}, \ \boldsymbol{D} = \begin{bmatrix} \boldsymbol{D}_{pp} & \boldsymbol{D}_{pT} \\ \boldsymbol{D}_{Tp} & \boldsymbol{K}_{TT}, \end{bmatrix} \tag{21}$$

where $\boldsymbol{R}_{int}$ and $\boldsymbol{R}_{ext}$ denote the internal and external force vectors, $\boldsymbol{\Delta d}$ is the increment of nodal vector of primary variables, $\boldsymbol{K}$ and $\boldsymbol{D}$ are the matrices resulting from the linearization of $\boldsymbol{R}_{int}$ with respect to the DOFs $\boldsymbol{d}$ and its temporal derivatives $\dot{\boldsymbol{d}}$ respectively. The complete details of the finite element formulation and implementation can be obtained from Zhou and Meschke (2013). This fully implicit Newton-Raphson scheme for the hydro-thermal problem suffers from numerical oscillations and convergence problems due to the sharp steepness and S-shaped of the liquid saturation curves as discussed by Dall'Amico et al. (2011). Therefore, the robustness of the Newton-Raphson scheme is improved by using the line search scheme for general unconstrained problems proposed by Pérez-Foguet and Armero (2002). In addition, for highly non-linear hydro-thermal problems the computational robustness can be further improved by means of semi-implicit treatment in time of the entropy balance, see the formulation in Appendix A.

2.3.1 Streamline Upwind/Petrov Galerkin (SUPG) stabilization for the entropy balance

The numerical simulation of ground freezing to control seepage flow is characterized by high Péclets numbers which results in non-physical oscillations of the temperature field, see Brooks and Hughes (1982), Hansen et al. (2019). Therefore, the entropy balance equation is stabilized employing SUPG to control non-physical oscillations. This results in the following stabilized weak form:

$$\begin{aligned}\delta W^2_{SUPG} = &\int_{\Gamma^{2\prime}_N} \delta T\, q^* \mathrm{d}A + \int_\Omega \delta T\, T\left(\frac{\mathrm{d}\, S_\mathrm{S}}{\mathrm{d}\, t} + \frac{\mathrm{d}\, m_\mathrm{C}}{\mathrm{d}\, t}(s_\mathrm{C} - s_\mathrm{L}) + m_\mathrm{L}\frac{\mathrm{d}\, s_\mathrm{L}}{\mathrm{d}\, t}\right.\\ &\left. + m_\mathrm{C}\frac{\mathrm{d}\, s_\mathrm{C}}{\mathrm{d}\, t}\right)\mathrm{d}V\\ &+ \int_\Omega \delta T\, T\, \boldsymbol{\nabla} \boldsymbol{s}_\mathrm{L}\cdot\boldsymbol{w}_\mathrm{L}\,\mathrm{d}V - \int_\Omega \boldsymbol{\nabla}\delta\boldsymbol{T}\cdot\boldsymbol{q}\,\mathrm{d}V - \int_\Omega \delta T\,\boldsymbol{\Phi}_M\,\mathrm{d}V\\ &+ \sum_{e=1}^{n_{el}}\int_{\Omega_e} \nabla\delta T\cdot\boldsymbol{w}_\mathrm{L}\tau_e\mathcal{L}\mathrm{d}V = 0,\end{aligned} \tag{22}$$

where n_{el} indicates the total numbers of elements in the discretized domain, Ω_e is the domain of the $e-$th element, and $\mathcal{L}$ is te residual defined as

$$\begin{aligned}\mathcal{L} =& T\left(\frac{\mathrm{d}\, S_\mathrm{S}}{\mathrm{d}\, t} + \frac{\mathrm{d}\, m_\mathrm{C}}{\mathrm{d}\, t}(s_\mathrm{C} - s_\mathrm{L}) + m_\mathrm{L}\frac{\mathrm{d}\, s_\mathrm{L}}{\mathrm{d}\, t} + m_\mathrm{C}\frac{\mathrm{d}\, s_\mathrm{C}}{\mathrm{d}\, t}\right)\\ &+ T\,\boldsymbol{\nabla}\boldsymbol{s}_\mathrm{L}\cdot\boldsymbol{w}_\mathrm{L} - \boldsymbol{\nabla}\cdot\boldsymbol{q} - \boldsymbol{\Phi}_M.\end{aligned} \tag{23}$$

The stabilization parameter τ_e is defined as

$$\tau_e = \frac{\alpha_e h_e}{2}\frac{1}{\|w_L\|} \text{ with } \alpha_e = \coth(\mathrm{Pe}) - \frac{1}{\mathrm{Pe}} \text{ and } \mathrm{Pe} = \frac{h_e c_L \|w_L\|}{2\lambda_L}, \tag{24}$$

where h_e is a characteristic length of the element and in this work is defined in 2D $h_e = \sqrt{2A_e}$ and 3D $h_e = \sqrt[3]{6V_e}$.

2.4 Numerical study of soil sample under freeze-thaw cycle: thermal analysis

In order to illustrate the effect of the unfrozen water content hysteresis model, a numerical study of a soil sample subjected to freeze-thaw cycle is conducted. The numerical study adopts the liquid saturation curves defined by the parameters given in Figs. 2(a) and 2(b). For the numerical study, a fully saturated cuboidal soil specimen with a height of 0.09 m and a cross-section of 0.41 × 0.41 m^2 at an initial temperature T_i = 10 °C is considered. The numerical analysis is performed in two stages. First stage or freezing phase, at time = 0 d, the top surface is instantaneously subjected to freezing with a constant heat flux q^* = −100 W/m^2. The second stage or thawing phase starts immediately after the average temperature of the sample reaches $T_{average} \approx -20$ °C. The second stage, at time = 1.875 d, the top surface is instantaneously subjected to heating with a constant heat flux q^* = 100 W/m^2. The simulation stops once the average temperature of the sample is $T_{average} \approx 10$ °C. All the other surfaces are kept thermally isolated during the whole analysis. The material parameters are listed in Table 1. In this numerical study, the temperature and liquid saturation at the monitoring point A are analyzed, see Fig. 4. Fig. 4(b) shows the effect of the consideration of freeze-thaw hysteresis. It is observed that during the thawing phase, the temperature at point A evolves upon different latent heats of thawing. This difference in temperature evolution is explained by the fact that the hysteresis model considers different values for the freezing point and thawing point which is not the case when freeze-thaw hysteresis is not considered. The analysis of the liquid saturation χ_L at point A shows that the complete thawing time for the soil specimen occurs according to the hysteretic model at t^B_{hys} = 3.48d and the non-hysteretic model at $t^B_{non-hys}$ = 3.40d, see Fig. 4 (d). Finally, monitoring point A reveals that the analysis considering the unfrozen water content hysteresis predicts slower thawing than the analysis that neglects it.

3 Model validation

3.1 Thawing of artificial ground freezing frozen wall: thermal analysis

In this section, a model test for the freeze-thaw cycle of soil is re-analyzed numerically. The test provides measurements for the evolution of the temperature field during the freezing and thawing process of a frozen wall, see Cai et al. (2023). The test consists of a box filled with saturated fine sand, shown in Fig. 5(a). A total of 3 pipes with a diameter of 10 mm are embedded in the sand and separated by a distance of 30 mm, see Fig. 5(b). The goal of the numerical study is the validation of the computational model in terms of the evolution of the temperature field under the freezing and thawing cycle. The numerical analysis is performed along the 2D section A-A shown in Fig. 5(a). The model set-up and initial conditions are depicted in Fig. 6(a). The temperatures on the pipes are prescribed according to the measurements on the pipe wall during freezing and thawing, see Fig. 6(b). The outer boundary of the domain is adiabatic, i.e., a zero heat flux is prescribed. The domain is meshed using 20 874 linear triangular elements, yielding a total of 10 593 degrees of freedom.

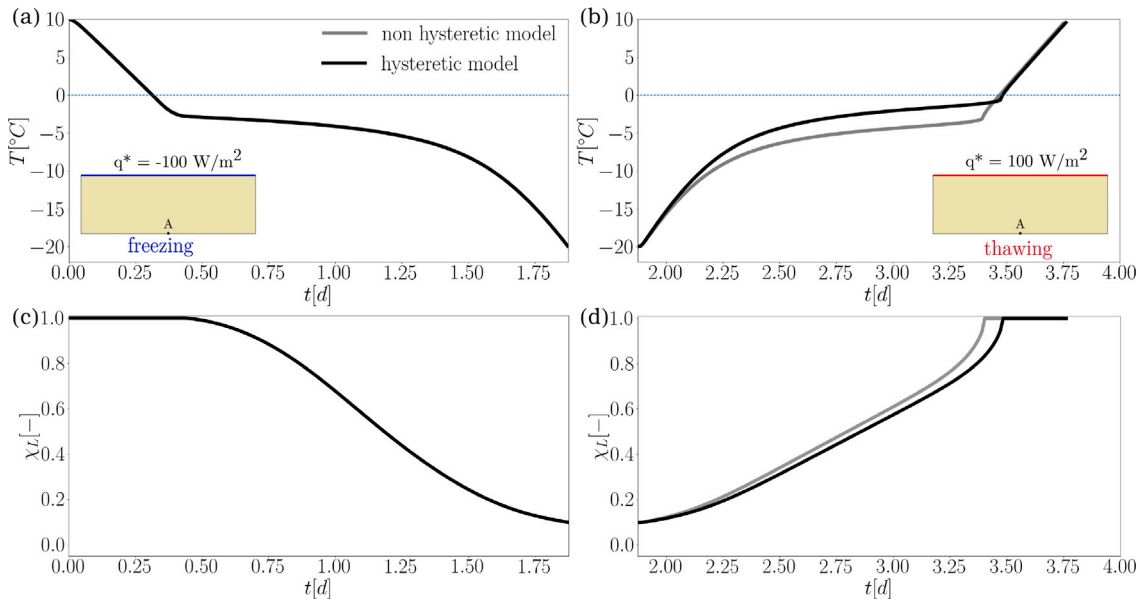

Fig. 4. Simulation of cuboidal soil specimen subjected to a freeze-thaw cycle. (a) Temperature evolution during the freezing phase at point A. (b) Temperature evolution during the thawing phase at point A. (c) Liquid saturation evolution during the freezing phase at point A. (d) Liquid saturation evolution during the thawing phase at point A.

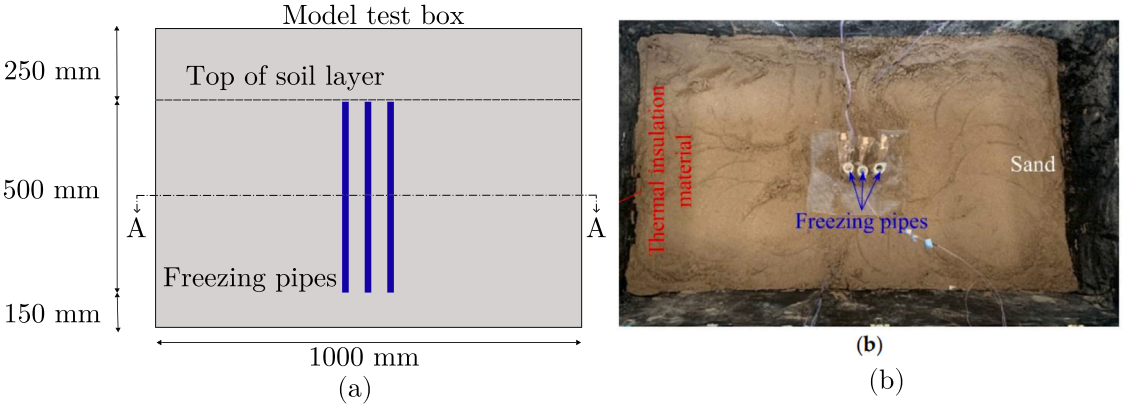

Fig. 5. Model test system for the freezing and thawing cycle of soil, see Cai et al. (2023). (a) 2D sketch of the model test box (b) Internal view of the model test box from Cai et al. (2023).

Table 2
Frozen wall numerical model: material properties of unfrozen and frozen soil.

	Initial Density	Heat capacity	Thermal conductivity	Porosity	Permeability	Freezing entropy
	ρ kg/m^3	c J/(kg K)	λ W/(m K)	ϕ –	κ m/s	S_f MPa/K
Sand	2700	705	2.1	0.44	0.0001	
Water	1000	4190	0.6	–	–	
Ice	917	2110	2.2	–	–	1.2

The total simulation time is $t = 157$ min with a constant time step of $\Delta t = 0.25$min. The reference material parameters of the sand layer are listed in Table B.10, which are used to calibrate the material parameters for the computational model, see Tables 2 and 3. During the freezing and thawing phase, in order to provide a validation of the computational model, a comparison between the computed and measured temperatures at the monitoring points T1 and T2 is presented in Fig. 6(c). It can be seen that the computed temperatures at the monitoring points T1 and T2 are in good qualitative agreement with the measurements during the freezing phase. Nevertheless, it can be seen that the computed temperatures evolve slower than the measured temperatures during the thawing phase, which is investigated in the following.

Table 3
Frozen wall numerical model: material properties of unfrozen liquid saturation model.

	T_f K	α_f –	m_f –	T_t K	α_t –	m_t –	$\chi_{L,u}$ –	$\chi_{L,res}$ –
Sand non-hysteresis	272.65	5	0.8	272.65	5	0.8	1.0	0.01
Sand hysteresis	272.65	5	0.8	273.025	5	0.85	1.0	0.01

3.1.1 Influence of the pipe temperature boundary conditions during the thawing phase

In this section, we study the prescribed pipe temperature as a potential contributing factor to the discrepancy observed between the

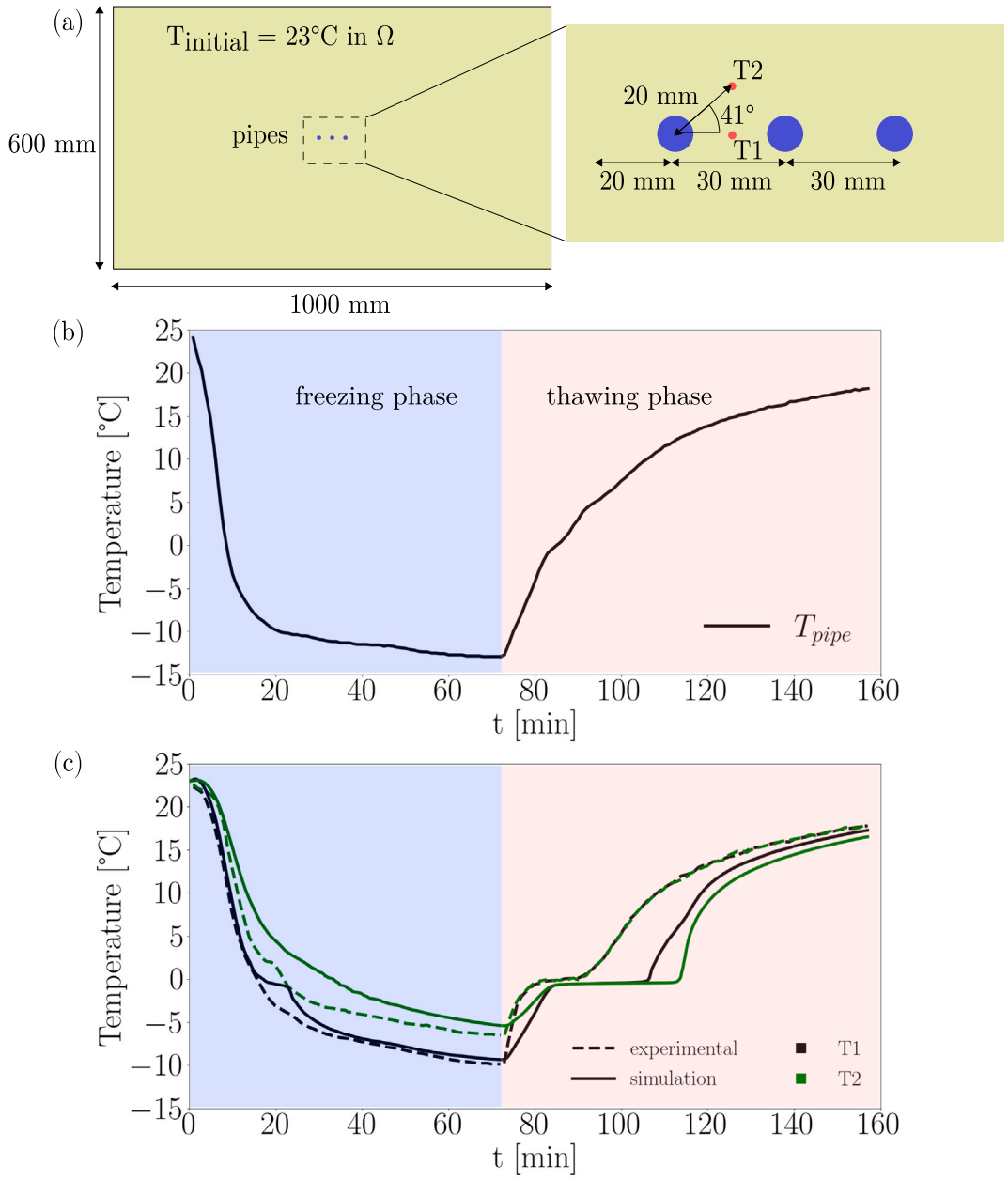

Fig. 6. Model set-up for fine sand subject to freeze-thaw cycle. (a) Geometry, initial conditions, freeze pipes and monitoring points T1 and T2. (b) Measured temperature boundary conditions on the pipe wall during a freezing–thawing cycle, from Cai et al. (2023). (c) Comparison of the temperature evolution at the monitoring points T1 and T2.

computed and measured temperatures during the thawing phase, especially during the phase transition of the sand layer. One possible explanation for the observed discrepancy is the presumption that the prescribed boundary condition does not extract heat from the frozen body fast enough. Therefore, the temperature boundary condition is adjusted in order to obtain a better agreement with the measurements, as shown in Fig. 7. It can be seen that the adjusted boundary conditions improve the qualitative agreement between the computed and measured temperatures during the phase transition.

3.1.2 Influence of the porosity during the phase transition of the frozen sand to unfrozen sand

The previous results show that the duration of the time interval in which the phase change from ice to water takes place is shorter in the experiment as compared to the simulation, see Fig. 7(b). During this interval the most dominant factors are the latent heat value of freezing, the amount of ice present in the soil pores and the thawing point of the ice. Therefore, the influence of porosity ϕ on the prediction of the duration of time interval in which the phase transition from the frozen sand to unfrozen sand layer is studied. The set $\phi = [0.25, 0.35, 0.44]$ is selected to be representative porosity values for sand. Results, shown in Fig. 8, show that the duration of the time interval where phase change of frozen sand to unfrozen sand takes place decreases with the decrease of the porosity and as a consequence the computed temperatures agrees better with the experimental measurements.

3.1.3 Influence of the unfrozen water content hysteresis on temperature during the thawing phase

The influence of the unfrozen water content hysteresis on temperature during the thawing phase is studied in this section. Results shows

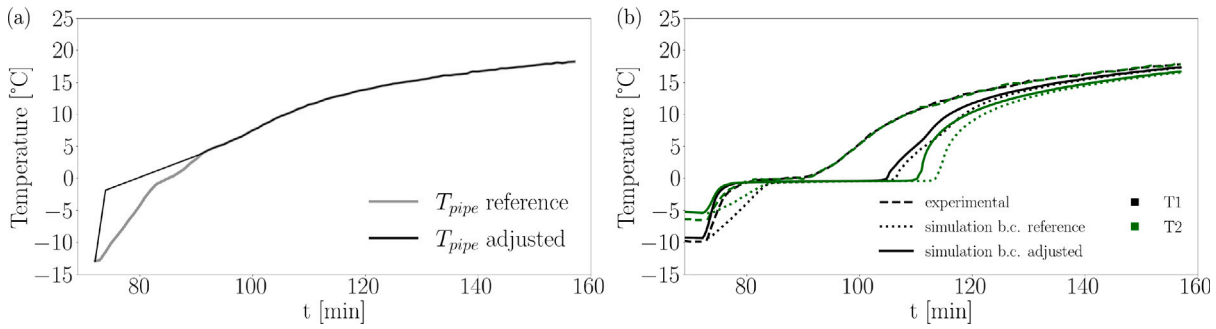

Fig. 7. Influence of the pipe temperature boundary conditions on the temperature prognosis during thawing. (a) Adjusted pipe temperature boundary conditions during thawing. (b) Comparison of temperature evolution at the monitoring points T1 and T2.

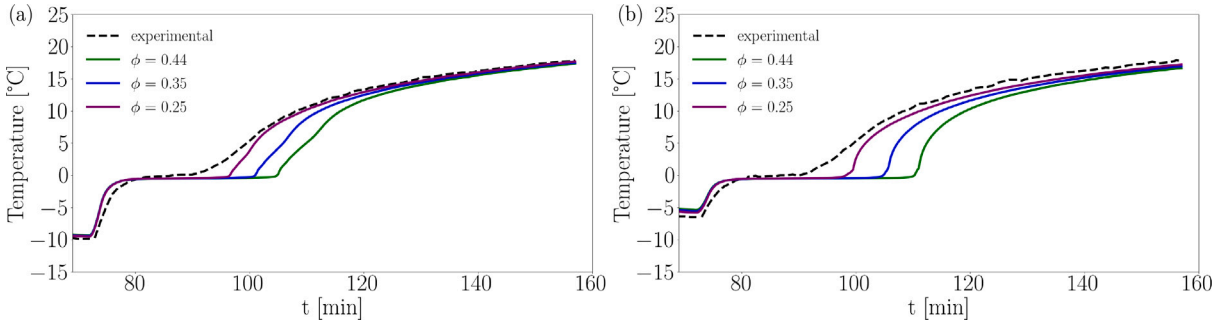

Fig. 8. Influence of the porosity on the temperature prognoses during thawing. (a) Comparison at monitoring point T1. (b) Comparison at monitoring point T2.

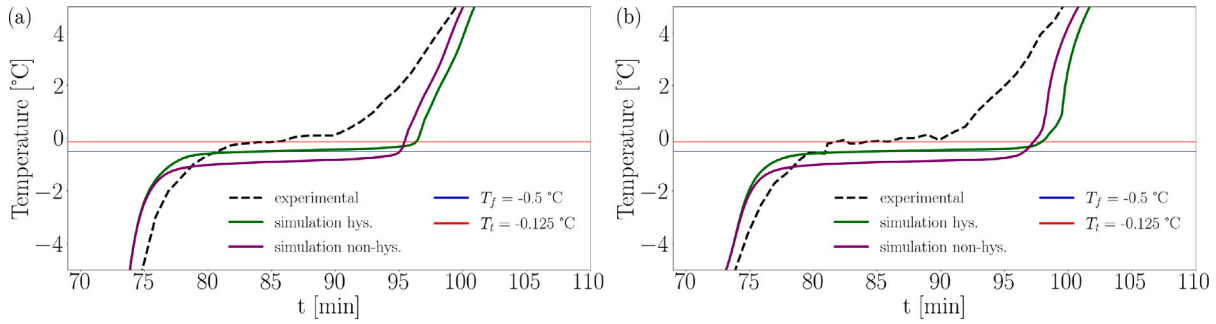

Fig. 9. Influence of the unfrozen water content freeze-thaw hysteresis on the temperature prognoses during thawing. (a) Comparison at monitoring point T1. (b) Comparison at monitoring point T2.

that the measured evolution of latent heat of the frozen sand agrees better with the temperature evolution predicted with consideration for unfrozen water content freeze-thaw hysteresis. This is explained by Figs. 9 (a) and 9 (b) where most of the latent heat occurs towards the thawing point $T_t = -0.125$ °C. In contrast, when hysteresis is disregarded, most of the latent heat occurs towards the freezing point $T_f = -0.5$ °C.

4 Numerical investigation of ground freezing in tunneling

In this section, three numerical case studies are presented which focus on the modeling of different applications of ground freezing in tunneling and consider the evolution of the unfrozen water content subjected to freezing or thawing for granular and cohesive soils. The numerical analysis covers the comparison between prediction and measurement of the temperature at monitoring points as well as the formation time and dimension of the frozen ground body. In addition, the forced thawing of the frozen soil is modeled with the goal of studying the influence of the unfrozen water content hysteresis on the prognoses of the thawing time in a large-scale engineering tunneling application.

4.1 Sequential artificial ground freezing during twin-tunnel construction: thermal analysis

In this section, a model test for artificial ground freezing is re-analyzed numerically. The test consists of the horizontal ground freezing of a twin tunnel, see Cai et al. (2019). The goal of the numerical analysis is the validation of the computational model in a boundary value problem in the context of artificial ground freezing in tunneling. The test set-up is depicted in Fig. 11. The twin tunnels are located in a sandy-silt soil layer, whose reference material parameters are listed in Table B.11. A total of 40 pipes with a diameter of 16 mm are installed in the physical model, where 20 freezing pipes are arranged around each tunnel, see Fig. 10(b). The freezing process is induced by circulating chilled brine with a lowered temperature of −30 °C. The test adopts a sequential freezing mode i.e. the downlink tunnel starts to freeze after the freezing and excavation of the uplink tunnel. The sequential freezing and excavation are divided into 4 stages. Namely, the first two stages consist of the freezing and excavation of the uplink tunnel with a duration of 225 min and 36 min, respectively. The third and fourth stages are concerned with the freezing and excavation of the downlink tunnel and have a duration of 195 min and 40 min, respectively. The

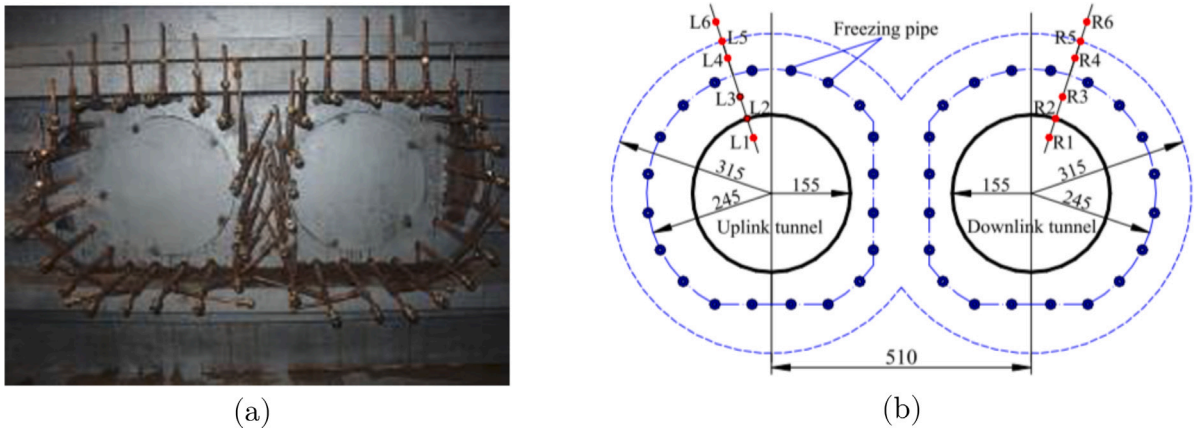

Fig. 10. Model test system for the sequential freezing and excavation of twin tunnels from Cai et al. (2019). (a) Freezing pipe arrangement. (b) Layout of freezing pipes and temperature measuring points (unit: mm).

Table 4
Twin tunnel numerical model: Material properties of unfrozen and frozen soil.

	Initial Density	Heat capacity	Thermal conductivity	Porosity	Freezing entropy
	ρ kg/m^3	c J/(kg K)	λ W/(m K)	ϕ –	S_f MPa/K
Sand	2700	730	1.8	0.5	
Water	1000	4190	0.6	–	
Ice	913	2095	2.22	–	1.2

Table 5
Twin tunnel numerical model: material properties of unfrozen liquid saturation model.

	T_f K	α_f –	m_f –	$\chi_{L,u}$ –	$\chi_{L,res}$ –
Sandy Silt	271.75	2	0.9	1.0	0.05

domain is meshed using 20 250 linear triangular elements, yielding a total of 10 165 degrees of freedom. The total simulation time is $t = 496$ min with a constant time step of $\Delta t = 1$ min. The material parameters for the computational model are listed in Table 4 and Table 5. The freezing is induced by prescribing on the pipes a constant temperature boundary condition of $T_{pipe} = -30$ °C. The results of the thermal analysis are shown in Fig. 11(b) at various time instants. The computed temperature and frozen wall thickness are compared with those obtained from the experiment. As shown in Fig. 11(b), the computed thickness of the frozen wall $w_{wall}^{simulation} \approx 85$ mm agrees with the measured frozen wall thickness $w_{wall}^{experiment} \approx 90$ mm at $t = 61$min, see Cai et al. (2019) . Similarly, during the third stage, the predicted thickness of the frozen soil $w_{wall}^{simulation} \approx 75$ mm agrees with the measured frozen wall thickness in the experiment $w_{wall}^{experiment} \approx 80$ mm at $t = 312$min as shown in Fig. 11(b), see Cai et al. (2019). In addition, a comparison is presented in Fig. 12 of the computed and measured temperatures at the monitoring points L3 and L4 located in the uplink tunnel and R3 and R4 located in the downlink tunnel.

4.1.1 Influence of constant and variable pipe temperature

Although the computed temperatures agree qualitatively with the experimental measurements, some quantitative deviations are present, an explanation for which concerns the assumption that the temperature on the freezing pipes is constant during the whole simulation. Experimental evidence shows, however, that the temperature on the pipe walls does not instantaneously reach the designed freezing temperature, see Sres (2009), Pimentel et al. (2012b) and Cai et al. (2023). In addition, the minimum temperature on the pipe walls can differ from the designed temperature because of heat loss as the coolant circulates through the pipe system, (Sres, 2009; Pimentel et al., 2012b). For this reason, the temperatures at the monitoring points L3, L4, R3 and R4 are re-calculated, where the pipe temperature during the freezing of the uplink and downlink tunnels is reduced with the help of the smooth function $T_{pipe}[t] = T_\infty + T_{delay}(\frac{t}{t_{ref}} - \frac{T_{delay}}{T_i - T_\infty})^{-1}$ depicted in Fig. 13(a). The parameters for the temperature function are: $t_{ref} = 3600$ s, $T_{delay} = 0.25$ °C, $T_\infty = -27$ °C and $T_i = 8$ °C. The computed temperatures using the smooth function agree more closely with the experimental measurements, as shown in Figs. 13(b) and 13(c). The enhancements in the results imply that for reliable prognoses information on the temperature on the pipe wall is essential.

4.2 Artificial ground freezing under seepage flow during twin-tunnel construction: Hydro-thermal analysis

This case study consists of the modeling of AGF in tunneling under seepage flow. The goal of the numerical analysis is the validation of the computational model in terms of temperature prediction under the influence of groundwater flow in a practical engineering scenario. The case study is based on the numerical experiment in Pimentel et al. (2012a) from a reference tunnel project in the German town of Fürth. According to the project description provided in Pimentel et al. (2012a), AGF was employed to control the groundwater flow perpendicularly to the tunnel with a velocity of 1.25 m/d. The reference geometry and material parameters of the case study are adopted from Pimentel et al. (2012a). The hydro-thermal numerical analysis is performed in 2D since the geometrical information provided in Pimentel et al. (2012a) was not enough to build a detailed 3D model. The average temperature history of the freeze pipes is considered as boundary conditions, see Fig. 14(b). The model set-up and initial conditions are shown in Fig. 15. The domain is meshed using 44 813 linear triangular elements for the temperature and water pressure fields, yielding a total of 22 695 degrees of freedom for each field. The total simulation time is $t = 40$ d with a constant time step of $\Delta t = 1$ h. The material parameters for the computational model are listed in Table 6 and Table 7, which are calibrated based on the reference material parameters from Table B.12. The results of the hydro-thermal analysis are shown in Fig. 16, where the computed temperature and ice

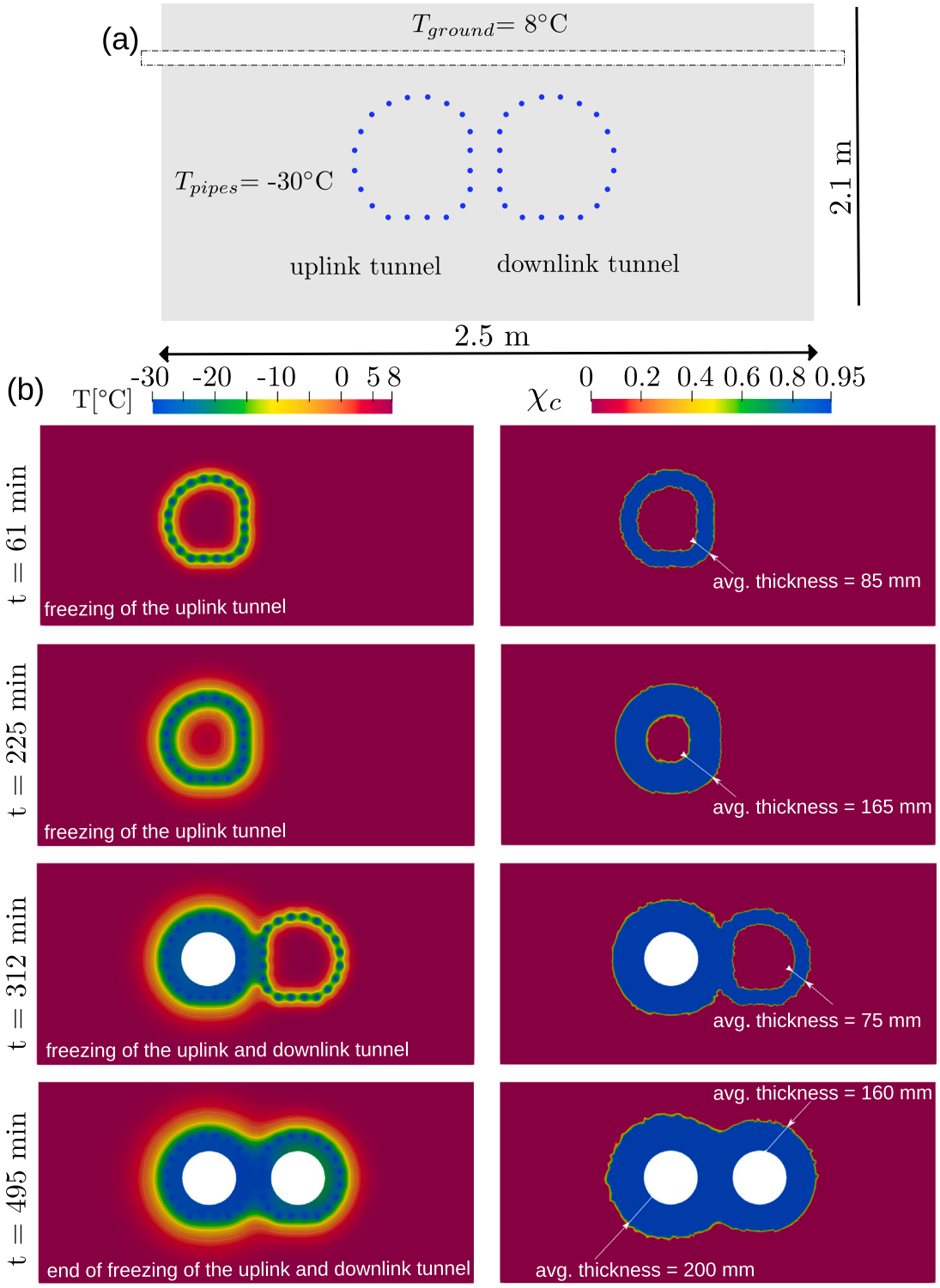

Fig. 11. Model test for horizontal ground freezing of twin tunnels. (a) Model set-up and initial conditions. (b) Temperature distribution, ice saturation distribution and thickness of the ice at different time instants during the freezing and excavation of the uplink and downlink tunnel.

saturation at different time steps are shown. The closure time of the frozen wall occurs at $t_{closure}$ = 15 d, which, however, differs from the closure time of the frozen wall $t^{ref}_{closure}$ = 28 d predicted by the numerical analysis in Pimentel et al. (2012a) and the closure time of $t^{ref}_{closure}$ = 24 d from in-situ observations. The disagreement can be explained by the fact that the analysis in this work is performed in 2D, whereas the analysis in Pimentel et al. (2012a) is in 3D and considers the inclination of the rock bed layer. Furthermore, the 2D analysis is unable to capture the changes of seepage flow perpendicular to the 2D frozen body cross section that occurs in a 3D simulation and can delay ice formation. Nevertheless, a good qualitative agreement is found in the comparison between the calculated temperatures and the measurements at the monitoring point T5 at various a cross-section of the frozen soil body, see Fig. 16(e) and Pimentel et al. (2012a).

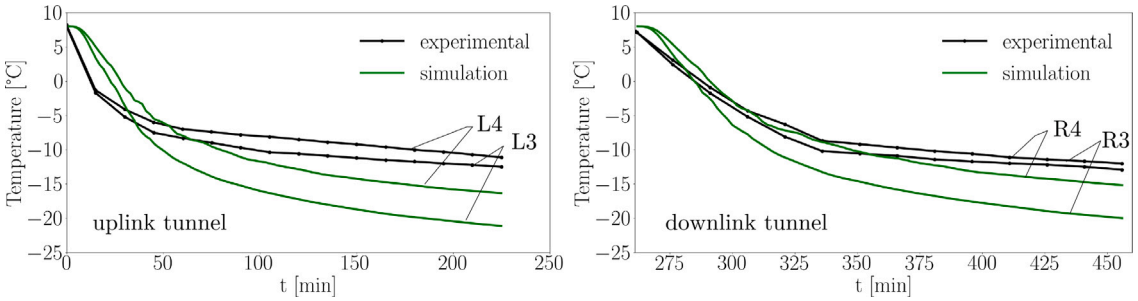

Fig. 12. Comparison of temperature evolution at the monitoring points considering constant pipe temperature. (a) Monitoring points L3 and L4 are located at the uplink tunnel. (b) Monitoring points R3 and R4 are located at the downlink tunnel.

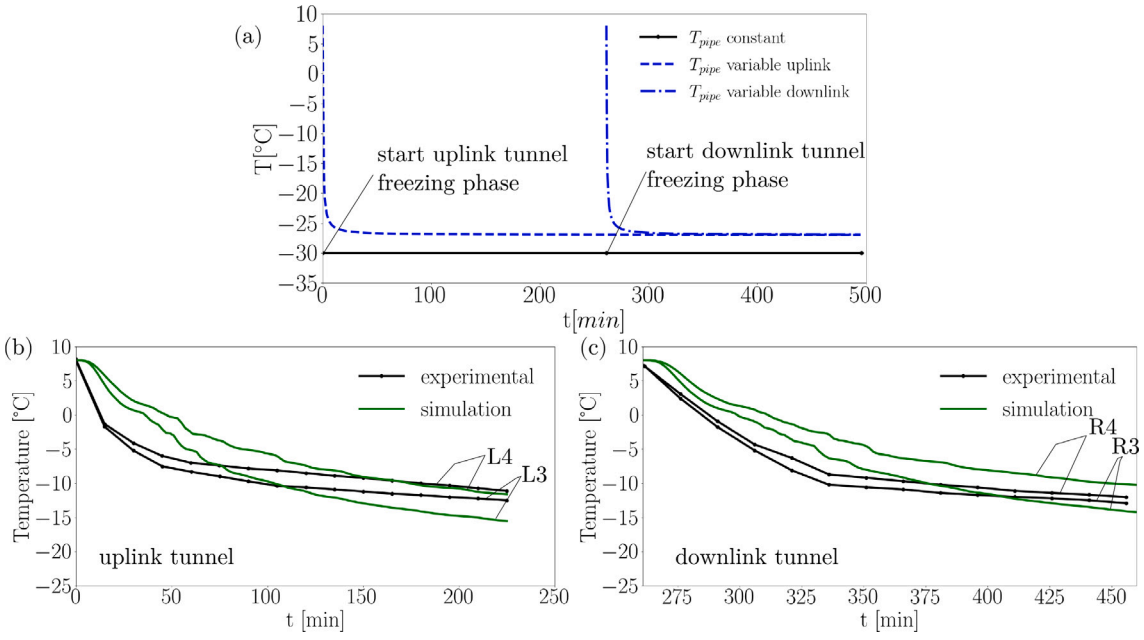

Fig. 13. Comparison of temperature evolution at the monitoring points considering variable pipe temperature. (a) Freeze pipes temperature during the freezing phase with decaying function with the parameters: t_{ref} = 3600 s, T_{delay} = 0.25 °C, T_{∞} = −27 °C and T_i = 8 °C. (b) Monitoring points L3 and L4 are located at the uplink tunnel. (c) Monitoring points R3 and R4 are located at the downlink tunnel.

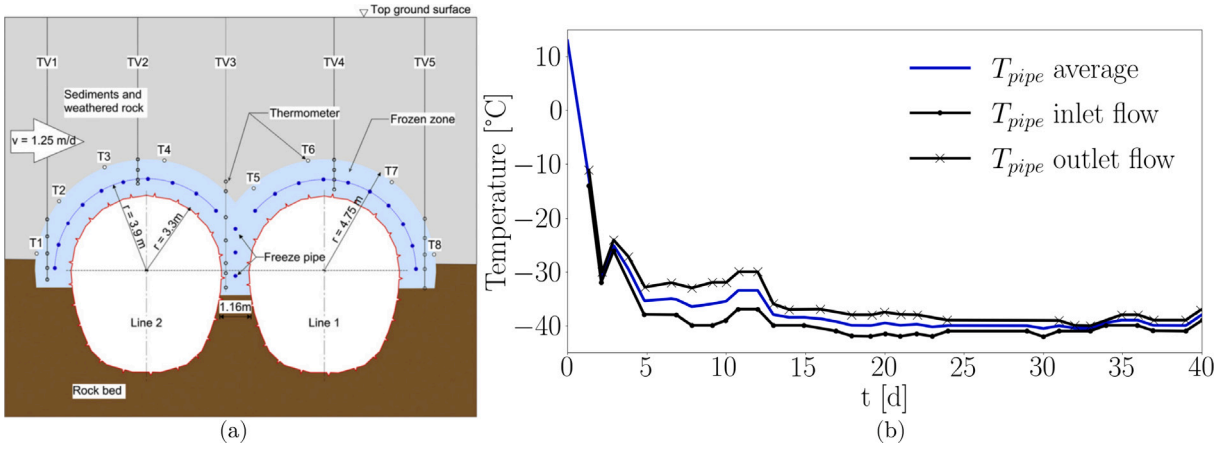

Fig. 14. AGF of twin-tunnel under seepage flow. (a) Reference geometry from Pimentel et al. (2012a). (b) Freeze pipe's temperature during the freezing phase data from Pimentel et al. (2012a).

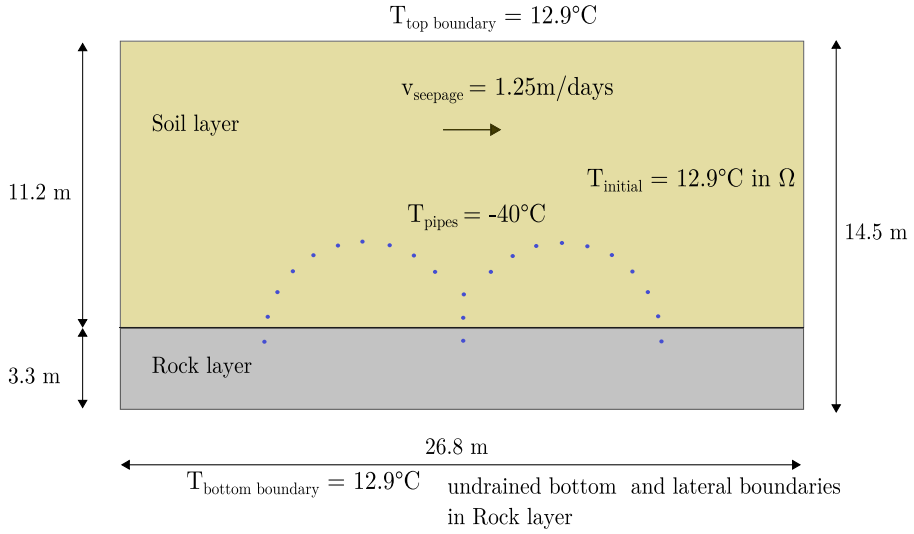

Fig. 15. Model set-up and initial conditions.

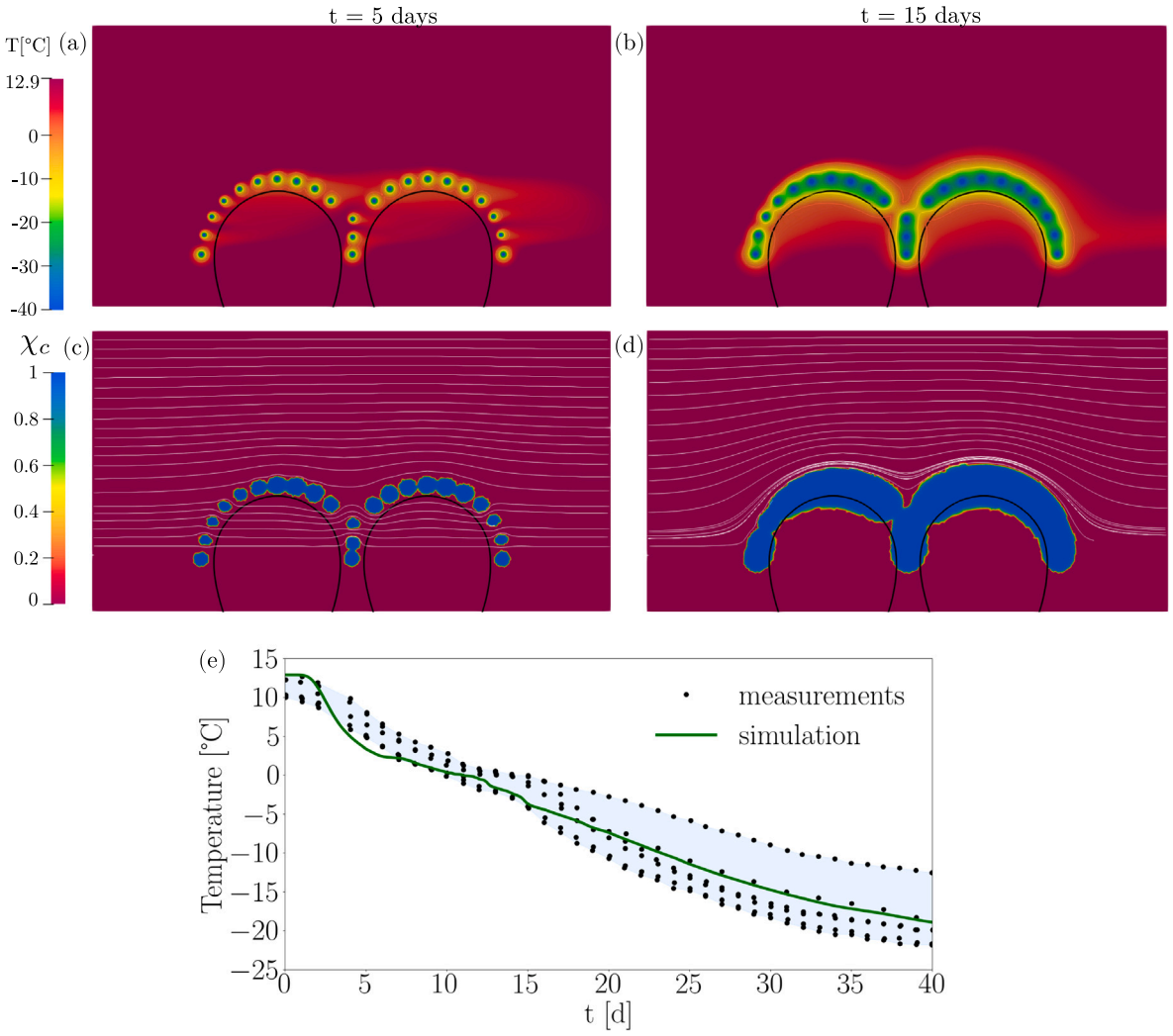

Fig. 16. Numerical simulation of ground freezing subject to seepage flow at different time instants. The boundary of the tunnel and the seepage streamlines are depicted in black and white lines respectively. (a) and (b) are the temperature distribution at 5 days and 15 days respectively. (c) and (d) are the ice saturation distribution at 5 d and at 15 days respectively. (e) Comparison of calculated temperatures and the envelop of the measurements at monitoring point T5 (see Fig. 14a) in Pimentel et al. (2012a).

Table 6
Twin tunnel under seepage flow numerical model: material properties of unfrozen and frozen ground.

	Initial Density	Heat capacity	Thermal conductivity	Porosity	Permeability	Freezing entropy
	ρ kg/m^3	c J/(kg K)	λ W/(m K)	ϕ –	κ m/s	S_f MPa/K
Sand	2650	750	4.34	0.36	1E−4	
Rock	2650	680	2.15	0.25	1E−14	
Water	1000	4190	0.6	–	–	
Ice	917	2100	2.2	–	–	1.2

* ϕ is back analyzed from GS and ρ.

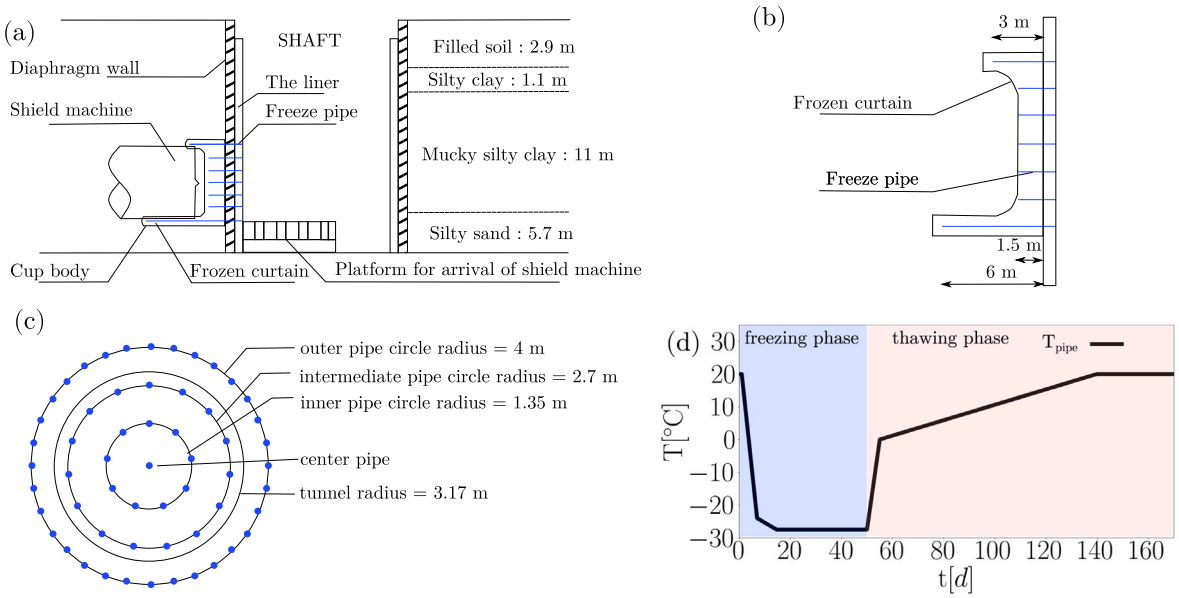

Fig. 17. Full face AGF for EPB shield tunneling see Fu et al. (2020). (a) Schematic of the cup-shaped ground freezing technique in shield tunneling. (b) The layout of the location of freeze pipes, and sectional view. (c) Layout of location of freeze pipes, elevation view. (d) Prescribed pipe temperature during freezing and thawing period.

Table 7
Twin tunnel under seepage flow numerical model: material properties of unfrozen liquid saturation model.

	T_f K	α_f –	m_f –	$\chi_{L,u}$ –	$\chi_{L,res}$ –
Sand	273.15	80	0.4	1.0	0.0
Rock	273.15	80	0.4	1.0	0.0

4.3 Thawing of cup-shaped artificial frozen soil in earth-pressure balance shield-driven tunneling: Hydro-thermal analysis

In this numerical case study, the freezing and thawing phases of a cup-shaped frozen body for full face soil strengthening for a shield driven tunnel in a layered soil stratum is numerically analyzed. This case study is inspired by the application of cup-shaped AGF intervention used for the reinforcement of the receiving shaft in the break-out of an earth-pressure balance shield tunneling machine, see Fu et al. (2020). The freeze pipe arrangement to create a cup-shaped body and the material parameters of the soil layers are adopted from Fu et al. (2020). The goal of this numerical case study is to investigate the thawing of the frozen soil in a scenario relevant to earth-pressure balance shield tunneling. In addition, we investigate the influence of the unfrozen water content freeze-thaw hysteresis on the prognoses of the thawing time of the frozen body. The model set-up and initial conditions are depicted in Fig. 18. The domain is discretized using 1 651 087 linear tetrahedral elements for the temperature and water pressure fields, yielding a total of 318 906 degrees of freedom for each field. The total time of the freezing and thawing process simulated in this study is $t = 170$ d with a constant time step of $\Delta t = 1$ d. The thermal material parameters for the computational model are listed in Table 8, which are calibrated based on the reference material parameters from Table B.13. Furthermore, the permeability and unfrozen water content of the soil layers are adopted from Saberi et al. (2021a), Tian et al. (2014) and listed in Tables 8 and 9.

The hydro-thermal numerical analysis is performed in 3D and consists of three stages. The first stage consists of the formation of a frost body by means of AGF. Consequently, the second stage consists of the simplified modeling of the heat sources in the tunnel interior during the shield advancement through the frost body. In addition, the surfaces inside the tunnel interior are considered impervious to water flow. Finally, the third stage comprises the modeling of the thawing of the cup-shaped frost body after the tunnel construction. According to the freezing schedule provided in Fu et al. (2020), the freezing process takes 50 d, see Fig. 17(d). The thawing phase which is induced by increasing the temperature on the pipes according to Fig. 17(d) is modeled immediately after the end of the freezing phase and takes 120 d. The numerical results of the freezing phase are shown in Fig. 19, where the formation of the cup-shaped frozen body at different time instances in the interval $\chi_C = [0.85, 1]$ is illustrated by means of the ice saturation iso-surfaces.

4.3.1 Forced thawing of the cup-shaped frozen body: influence of the unfrozen water content hysteresis

In order to investigate the influence of the unfrozen water content freeze-thaw hysteresis on the prognosis, the thawing evolution of the cup-shape frozen body is analyzed in Fig. 20, where elements with ice saturation $\chi_C > 0.3$ at the end of the freezing phase are shown

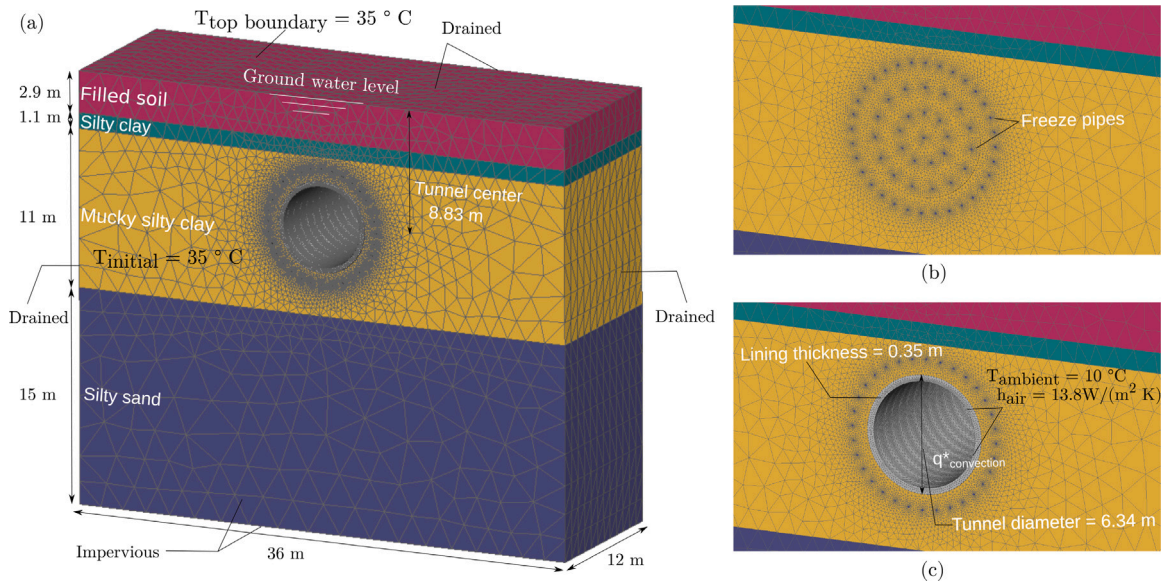

Fig. 18. Model set-up for hydro-thermal analysis. (a) 3D view of the mesh of the soil layers and the excavated tunnel. (b) 2D view of the location of the freeze pipes on the mesh before excavation. (c) 2D view of the mesh of the constructed tunnel.

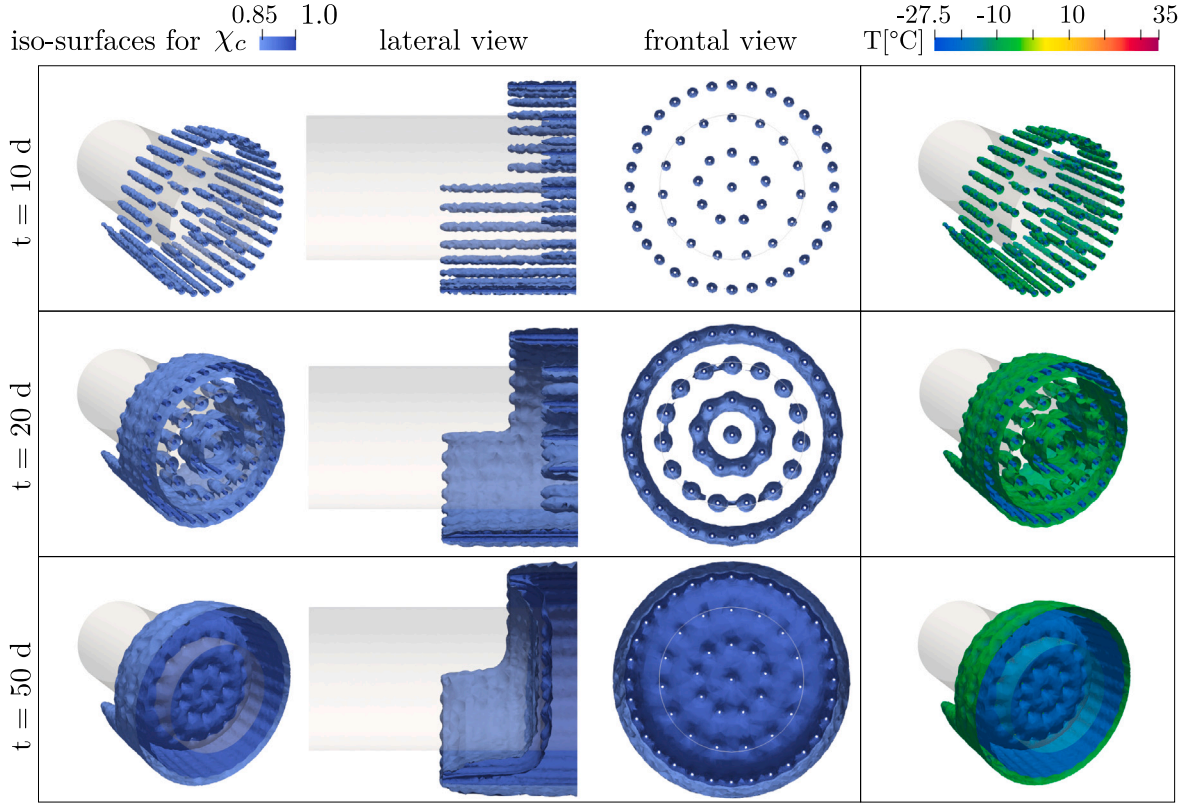

Fig. 19. Numerical analysis of the ice formation during the active freezing phase of the cup-shaped frozen body by means of the ice saturation iso-surfaces. The iso-surfaces are generated for a range of ice saturation χ_L = [0.85, 1] (a). 3D view and 2D sections of the ice saturation iso-surfaces at different time instants. (b) Temperature distribution visualized on the ice saturation iso-surfaces at different time instants.

with and without consideration for hysteresis. Although the influence of hysteresis on the results is discernible already at t = 76 d, it is more clearly visible at time t = 78 d, where a significantly smaller portion of the frozen soil has thawed in the simulation with hysteresis in comparison with its non-hysteresis counterpart. The final thawing time of the cup-shaped frozen body is predicted to be t_{hys} = 82 d and $t_{non-hys}$ = 79 d with and without hysteresis, respectively. It can be seen that consideration for hysteresis can have a decisive effect on the simulation results, highlighted by the 3d difference in the total thawing time, where the thawing of the frozen body is slower in the presence of hysteresis.

Table 8
Thawing of cup-shaped artificial frozen soil: material properties of unfrozen, frozen soil and concrete lining.

	Initial Density	Heat capacity	Thermal conductivity	Porosity	Permeability	Freezing entropy
	ρ kg/m^3	c J/(kg K)	λ W/(m K)	ϕ –	κ m/s	S_f MPa/K
Filled soil	2650	821	2.36	0.46	1E−4	
Silty clay	2650	900	2.47	0.46	1E−6	
Mucky silty clay	2650	705	2.03	0.54	1E−7	
Silty sand	2650	758	3.58	0.43	1E−5	
Water	1000	4190	0.6	–	–	
Ice	917	2110	2.2	–	–	1.2
Concrete lining	2400	913	1.36	–	–	–

Table 9
Thawing of cup-shaped artificial frozen soil: material properties of unfrozen liquid saturation model.

	T_f K	α_f –	m_f –	T_t K	α_t –	m_t –	$\chi_{L,u}$ –	$\chi_{L,res}$ –
Filled soil non-hysteresis	−2.75	0.5	0.82	−0.25	0.5	0.82	1.0	0.03
Filled soil hysteresis	−2.75	0.5	0.82	−0.25	0.5	0.82	1.0	0.03
Silty clay non-hysteresis	−2.8	0.35	0.84	−0.25	0.35	0.8	1.0	0.05
Silty clay hysteresis	−2.8	0.35	0.84	−0.25	0.35	0.8	1.0	0.05
Mucky silty clay non-hysteresis	−2.8	0.35	0.84	−0.25	0.35	0.8	1.0	0.05
Mucky silty clay hysteresis	−2.8	0.35	0.84	−0.25	0.35	0.8	1.0	0.05
Silty sand non-hysteresis	−2.75	0.5	0.82	−0.25	0.5	0.82	1.0	0.03
Silty sand hysteresis	−2.75	0.5	0.82	−0.25	0.5	0.82	1.0	0.03

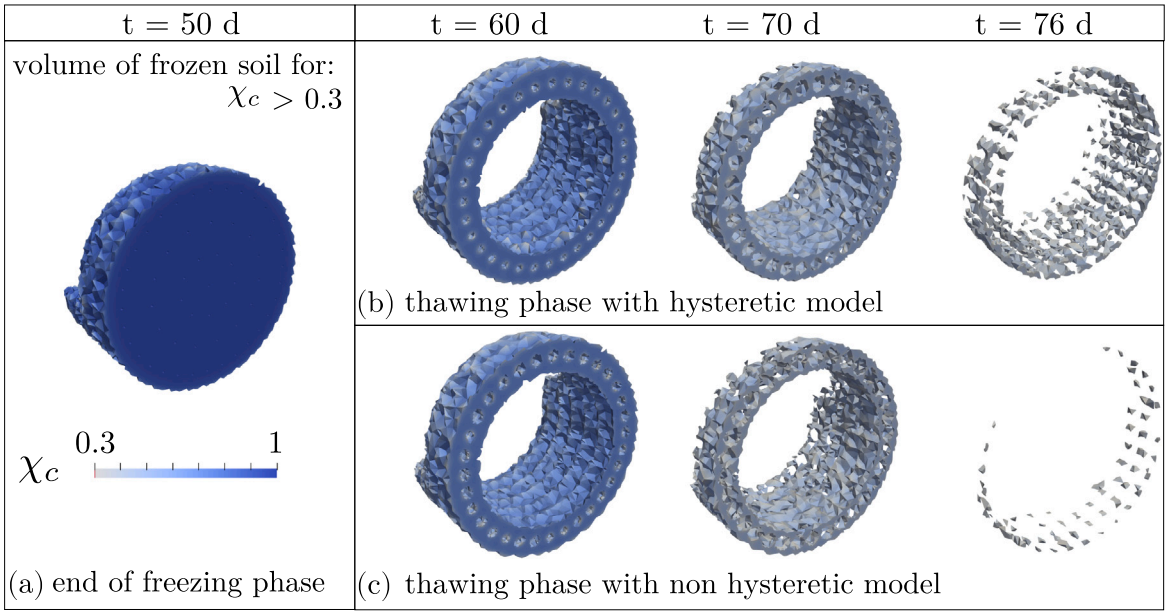

Fig. 20. Frozen soil volume for values of ice saturation $\chi_C > 0.3$. (a) Volume of frozen soil at the end of the freezing phase at $t = 50$ d. (b) The volume of frozen soil during the thawing phase at $t = 60$ d, $t = 70$ d and $t = 76$ d.

5 Conclusions

In this work, we presented a coupled thermo-hydraulic finite element computational model for the freezing and thawing of soils, which included the hysteresis behavior of the unfrozen liquid content. The model was validated by the numerical reanalysis of the freezing and thawing of a frozen wall in the model test from Cai et al. (2023). Results showed that the incorporation of hysteresis response in the unfrozen water content under freeze-thaw cycle leads to longer thawing times in comparison to the case where hysteresis is disregarded. It was also found that consideration of hysteresis leads to a better agreement with the experimental data.

Furthermore, the presented computational model was used to analyze three boundary-value problems of artificial ground freezing in tunneling. It was found from the first study, which focused on the temperature profile during sequential freezing in a twin tunnel construction (Cai et al., 2019), that for reliable prognoses, the appropriate description of pipe temperatures is crucial, a finding, which is also supported by Pimentel et al. (2012a). It was shown that, in addition to the temperature evolution, the model predictions agreed the average thickness of the frozen arch at different time instants. The second study was characterized by the thermo-hydraulic analysis of artificial ground freezing under seepage flow during the construction of a twin tunnel in Fürth (Pimentel et al., 2012a). It was found that notwithstanding minor differences concerning the ice formation time, the model was in good agreement with field measurements, highlighting the usability of the presented computational model for the coupled thermo-hydraulic process on the structural scale. We focused on the forced thawing of the cup-shaped frozen zone in shield tunneling in the third example. It was found that the unfrozen water content hysteresis in the freezing and

thawing processes plays a significant role in the prognosis of the model, where the predicted thawing time differed up to 3 days depending on whether hysteresis was considered.

The obtained results indicate that the presented computational model is capable of providing a relevant prognosis for the coupled thermo-hydraulic processes of ground freezing in tunneling. The hysteresis response of the unfrozen liquid content during the freezing and thawing cycle was, furthermore, seen to have a marked influence on the entire thermo-hydraulic process, which can consequently manifest itself in structural-scale metrics such as the thawing time.

CRediT authorship contribution statement

R.J. Williams M.: Writing – original draft, Software. **M. Saberi:** Writing – review & editing, Software. **G. Meschke:** Writing – review & editing, Supervision.

Declaration of competing interest

The authors declare that they have no known competing financial interests or personal relationships that could have appeared to influence the work reported in this paper.

Data availability

No data was used for the research described in the article.

Acknowledgments

This research is funded by the Deutsche Forschungsgemeinschaft (DFG, German Research Foundation) – Project number: 77309832 within Subproject C1 of the Collaborative Research Center SFB 837 "Interaction modeling in Mechanised tunneling". The authors also would like to acknowledge the numerous helpful discussions with Dr. W. Orth (Dr.-Ing. Orth GmbH) and Prof. M. Thewes (Ruhr University Bochum), which considerably helped to focus and improve the validation and the modeling strategy. Finally, the authors would like to acknowledge Dr. C. König (delta h Ingenieurgesellschaft mbH) who initiated and supported the development of the hysteresis model.

Appendix A. Semi-implicit treatment in time of the entropy balance

The fully discretized variational forms of the hydro-thermal problem evaluated at the generalized midpoint can be written according to Zhou and Meschke (2013).

$$\begin{aligned}\delta W^1_{n+1-\alpha} = &\bigcup_e^{\mathrm{NE}} \sum_i^{\mathrm{NN}^q} (\delta p^e_{\mathrm{L}i})_{n+1-\alpha} \left\{ \int_{\Gamma^{e2}_N} N^l_i \, w^* \, \mathrm{d}A \right. \\ &- \sum_j^3 \int_{\Omega^e} N^l_{i;j} \, \left((w_{\mathrm{L}})_j\right)_{n+1-\alpha} \mathrm{d}V \\ &\left. + \int_{\Omega^e} N^l_i \left(\frac{\partial\,(m_{\mathrm{L}}+m_{\mathrm{C}})}{\partial\, p_{\mathrm{L}}} \dot{p_{\mathrm{L}}} + \frac{\partial\,(m_{\mathrm{L}}+m_{\mathrm{C}})}{\partial\, T} \dot{T} \right)_{n+1-\alpha} \mathrm{d}V \right\} \\ = &(\boldsymbol{\delta p}_{\mathrm{L}})_{n+1-\alpha} \cdot \left\{ \boldsymbol{R}^1_{\mathrm{ext}} + \boldsymbol{R}^1_{\mathrm{int}} \right\}_{n+1-\alpha} = 0 \,. \end{aligned} \tag{A.1}$$

$$\begin{aligned}\delta W^2_{n+1-\alpha} = &\bigcup_e^{\mathrm{NE}} \sum_i^{\mathrm{NN}^q} (\delta T^e_i)_{n+1-\alpha} \left\{ \int_{\Gamma^{e3}_N} N^l_i \, q^* \mathrm{d}A - \sum_j^3 \int_{\Omega^e} N^l_{i;j} \, (q_j)_{n+1-\alpha} \mathrm{d}V \right. \\ &+ \int_{\Omega^e} N^l_i \left(T \left(\frac{\partial\, S_{\mathrm{S}}}{\partial\, p_{\mathrm{L}}} + \frac{\partial\, m_{\mathrm{C}}}{\partial\, p_{\mathrm{L}}} (s_{\mathrm{C}} - s_{\mathrm{L}}) + m_{\mathrm{L}} \frac{\partial\, s_{\mathrm{L}}}{\partial\, p_{\mathrm{L}}} \right. \right. \\ &\left. \left. + m_{\mathrm{C}} \frac{\partial\, s_{\mathrm{C}}}{\partial\, p_{\mathrm{L}}} \right) \dot{p_{\mathrm{L}}} \right)_{n+1-\alpha} \mathrm{d}V \\ &+ \int_{\Omega^e} N^l_i \left(T \left(\frac{\partial\, S_{\mathrm{S}}}{\partial\, T} + \frac{\partial\, m_{\mathrm{C}}}{\partial\, T} (s_{\mathrm{C}} - s_{\mathrm{L}}) + m_{\mathrm{L}} \frac{\partial\, s_{\mathrm{L}}}{\partial\, T} \right. \right. \\ &\left. \left. + m_{\mathrm{C}} \frac{\partial\, s_{\mathrm{C}}}{\partial\, T} \right) \dot{T} \right)_{n+1-\alpha} \mathrm{d}V \\ &+ \sum_j^3 \int_{\Omega^e} N^l_i \left(T \left(\frac{\partial\, s_{\mathrm{L}}}{\partial\, p_{\mathrm{L}}} (\nabla p_{\mathrm{L}})_j + \frac{\partial\, s_{\mathrm{L}}}{\partial\, T} \nabla T_j \right) (w_{\mathrm{L}})_j \right)_{n+1-\alpha} \mathrm{d}V \\ &\left. - \int_{\Omega^e} N^l_i \, (\boldsymbol{\Phi}_M)_{n+1-\alpha} \, \mathrm{d}V \right\} \\ = &(\boldsymbol{\delta T})_{n+1-\alpha} \cdot \left\{ \boldsymbol{R}^2_{\mathrm{ext}} + \boldsymbol{R}^2_{\mathrm{int}} \right\}_{n+1-\alpha} = 0 \,. \end{aligned} \tag{A.2}$$

In compact notation, the discretized weak form can be formulated as

$$\delta W_{n+1-\alpha} = (\boldsymbol{\delta d})_{n+1-\alpha} \cdot \left\{ \boldsymbol{R}_{\mathrm{ext}} + \boldsymbol{R}_{\mathrm{int}} \right\}_{n+1-\alpha} = 0 \,, \tag{A.3}$$

where $\boldsymbol{R}_{\mathrm{ext}}$ and $\boldsymbol{R}_{\mathrm{int}}$ are external and internal force vectors, respectively. When the parameters $\alpha_m = \alpha_f = \frac{1}{2}$, $\beta = \frac{1}{4}$ and $\gamma = \frac{1}{2}$ are used the semi discretized Eqs. (A.3) forms a fully implicit scheme. This discretized forms are highly non-linear due to the strong hydro-thermal coupling of the constitutive relations specially when the soil pore water undergoes to phase-change from liquid-water to ice or vice versa. For the sake of increasing the robustness of the computational model, the highly non-linearity of the hydro-thermal problem is reduced using a semi-implicit treatment in time of the entropy balance equation (A.2) and it is written as follows:

$$\begin{aligned}\delta \bar{W}^2_{n+1-\alpha} = &\bigcup_e^{\mathrm{NE}} \sum_i^{\mathrm{NN}^q} (\delta T^e_i)_{n+1-\alpha} \left\{ \int_{\Gamma^{e3}_N} N^l_i \, q^* \mathrm{d}A \right. \\ &- \sum_j^3 \int_{\Omega^e} N^l_{i;j} \, (q_j)_{n,\,n+1-\alpha} \mathrm{d}V \\ &+ \int_{\Omega^e} N^l_i \left(T_{n+1-\alpha} \left(\frac{\partial\, S_{\mathrm{S}}}{\partial\, p_{\mathrm{L}}} + \frac{\partial\, m_{\mathrm{C}}}{\partial\, p_{\mathrm{L}}} (s_{\mathrm{C}} - s_{\mathrm{L}}) + m_{\mathrm{L}} \frac{\partial\, s_{\mathrm{L}}}{\partial\, p_{\mathrm{L}}} \right. \right. \\ &\left. \left. + m_{\mathrm{C}} \frac{\partial\, s_{\mathrm{C}}}{\partial\, p_{\mathrm{L}}} \right) \Big|_n \dot{p}_{\mathrm{L}n+1-\alpha} \right) \mathrm{d}V \\ &+ \int_{\Omega^e} N^l_i \left(T_{n+1-\alpha} \left(\frac{\partial\, S_{\mathrm{S}}}{\partial\, T} + \frac{\partial\, m_{\mathrm{C}}}{\partial\, T} (s_{\mathrm{C}} - s_{\mathrm{L}}) + m_{\mathrm{L}} \frac{\partial\, s_{\mathrm{L}}}{\partial\, T} \right. \right. \\ &\left. \left. + m_{\mathrm{C}} \frac{\partial\, s_{\mathrm{C}}}{\partial\, T} \right) \Big|_n \dot{T}_{n+1-\alpha} \right) \mathrm{d}V \\ &+ \sum_j^3 \int_{\Omega^e} N^l_i \left(T_{n+1-\alpha} \left(\frac{\partial\, s_{\mathrm{L}}}{\partial\, p_{\mathrm{L}}} \Big|_n (\nabla p_{\mathrm{L}})_j \Big|_n + \frac{\partial\, s_{\mathrm{L}}}{\partial\, T} \Big|_n (\nabla T_j)_{n+1-\alpha} \right) \right. \\ &\left. (w_{\mathrm{L}})_j \Big|_n \right) \mathrm{d}V \\ &\left. - \int_{\Omega^e} N^l_i \, (\boldsymbol{\Phi}_M) \Big|_n \, \mathrm{d}V \right\} \\ = &(\boldsymbol{\delta T})_{n+1-\alpha} \cdot \left\{ \boldsymbol{R}^2_{\mathrm{ext}} + \bar{\boldsymbol{R}}^2_{\mathrm{int}} \right\}_{n+1-\alpha} = 0 \,. \end{aligned} \tag{A.4}$$

where $(q_j)_{n,\,n+1-\alpha} = -\lambda_{tot} \Big|_n (\nabla T_j)_{n+1-\alpha}$ and $(\cdot) \Big|_n$ denotes the use of the last converged primary variables T_n and $(p_{\mathrm{L}})_n$ at the time step t_n.

Appendix B. Material parameters used for back analysis

B.1. Thawing of artificial ground freezing frozen wall: thermal analysis

See Table B.10.

B.2. Sequential artificial ground freezing during twin-tunnel construction: thermal analysis

See Table B.11.

B.3. Artificial ground freezing under seepage flow during twin-tunnel construction: hydro-thermal analysis

See Table B.12.

Table B.10
Frozen wall model test: material properties of soil layer.

Sand	Density	Specific gravity	Porosity	Heat capacity	Thermal conductivity
	ρ kg/m^3	GS –	ϕ –	c J/(kg K)	λ W/(m K)
unfrozen	1950	2.7	0.44 *	1493	1.11
frozen	–	–	–	1004	1.84

* ϕ is back analyzed from GS and ρ.

Table B.11
Twin tunnel model test: material properties of soil layers.

Material	Density	Specific gravity	Porosity	Heat capacity	Thermal conductivity
	ρ_{sat} kg/m^3	GS –	ϕ –	c J/(kg K)	λ W/(m K)
Sandy silt unfrozen	1837	2.7	0.5 *	1230	1.51
Sandy silt frozen	–	–	–	1523	1.35

* ϕ is back analyzed from GS and ρ_{sat}.

Table B.12
Twin tunnel under seepage flow: material properties of soil layers.

Material	Density	Heat capacity	Thermal conductivity
	ρ_{dry} kg/m^3	c_{vol} MJ/(m^3 K)	λ W/(m K)
Sand unfrozen	1700	2.78	2.20
Sand frozen	–	2.03	3.40
Rock unfrozen	2000	2.4	2.0
Rock frozen	–	1.95	2.16

Table B.13
Natural thawing of frozen soil: material properties of soil layer.

Material	Density	Heat capacity	Thermal conductivity
	ρ_{dry} kg/m^3	c J/(/kg K)	λ W/(m K)
Filled soil unfrozen	1440	1506	1.34
Filled soil frozen	–	1250	2.12
Silty clay unfrozen	1430	1547	1.35
Silty clay frozen	–	1330	2.22
Mucky silty clay unfrozen	1215	1717	1.06
Mucky silty clay frozen	–	1321	2.10
Silty sand unfrozen	1505	1473	1.87
Silty sand frozen	–	1083	2.50

B.4. Thawing of cup-shaped artificial frozen soil in shield-driven tunneling: hydro-thermal analysis

See Table B.13.

References

Anderson, D.M., Tice, A.R., 1972. Predicting unfrozen water contents in frozen soils from surface area measurements. Highway research record 393 (2), 12–18.

Baier, C., 2008. Thermisch-hydraulische Simulationen zur Optimierung von Vereisungsma?ahmen im Tunnelbau unter Einfluss einer Grundwasserstr?mung (Ph.D. thesis). rwth-aachen, Aachen, XII, 168 Bl. : Ill., graph. Darst., URL https://publications.rwth-aachen.de/record/50659, Aachen, Techn. Hochsch., Diss., 2008.

Birgersson, M., Karnland, O., Nilsson, U., 2010. Freezing of bentonite - experimental studies and theoretical considerations. SKB Tech. Rep. 50, URL http://www.skb.se/upload/publications/pdf/TR-10-40.pdf.

Bittelli, M., Flury, M., Campbell, G.S., 2003. A thermodielectric analyzer to measure the freezing and moisture characteristic of porous media. Water Resour. Res. 39 (2).

Black, P.B., 1995. Applications of the Clapeyron equation to water and ice in porous media. Cold Regions Research and Engineering Laboratory (US).

Bluhm, J., Ricken, T., 2007. Modeling of freezing and thawing processes in liquid filled thermo-elastic porous solids. In: Setzer, M. (Ed.), Proceeding of the 5Th International Conference on Transport in Concrete. pp. 41–57.

Bonetti, E., Fremond, M., 2003. A phase transition model with the entropy balance. Math. Methods Appl. Sci. 26, 539–556.

Brooks, A., Hughes, T., 1982. Streamline upwind/Petrov-Galerkin formulations for convection dominated flows with particular emphasis on the incompressible Navier-Stokes equations. Comput. Methods Appl. Mech. Engrg. 32 (1), 199–259. http://dx.doi.org/10.1016/0045-7825(82)90071-8.

Cai, H., Li, S., Liang, Y., Yao, Z., Cheng, H., 2019. Model test and numerical simulation of frost heave during twin-tunnel construction using artificial ground-freezing technique. Comput. Geotech. 115, http://dx.doi.org/10.1016/j.compgeo.2019.103155.

Cai, H., Yang, L., Pang, C., Li, M., Lu, C., Hong, R., 2023. Model test study on natural thawing temperature field of artificial ground frozen wall. Sustainability 15 (4), http://dx.doi.org/10.3390/su15043186, URL https://www.mdpi.com/2071-1050/15/4/3186.

Côté, J., Konrad, J.-M., 2005. A generalized thermal conductivity model for soils and construction materials. Can. Geotech. J. 42 (2), 443–458. http://dx.doi.org/10.1139/t04-106.

Coussy, O., 2005. Poromechanics of freezing materials. J. Mech. Phys. Solids 53, 1389–1718.

Dadvand, P., Rossi, R., Oñate, E., 2010. An object-oriented environment for developing finite element codes for multi-disciplinary applications. Arch. Comput. Methods Eng. 17, 253–297.

Dall'Amico, M., Endrizzi, S., Gruber, S., Rigon, R., 2011. A robust and energy-conserving model of freezing variably-saturated soil. Cryosphere 5, 469–484. http://dx.doi.org/10.5194/tc-5-469-2011.

de Boer, R., 2000. Theory of Porous Media - highlights in the historical development and current state, vol. 2, Springer-Verlag, Berlin, Heidelberg, New York.

Ehlers, W., 1989. Poröse medien, ein kontinuumsmechanisches modell auf der basis der mischungstheorie. Technical Report, Universität Gesamthochschule Essen.

Fu, Y., Hu, J., Liu, J., Hu, S., Yuan, Y., Zeng, H., 2020. Finite Element Analysis of Natural Thawing Heat Transfer of Artificial Frozen Soil in Shield-Driven Tunnelling. Adv. Civil Eng. 2020, http://dx.doi.org/10.1155/2020/2769064.

Grant, S., 2000. Physical and chemical factors affecting contaminant hydrology in cold enviroment. ERDC/CRREL TR-00-21, US Army Corps of Engineers.

Hansen, K.B., Arzani, A., Shadden, S.C., 2019. Finite element modeling of near-wall mass transport in cardiovascular flows. Int. J. Numer. Methods Biomed. Eng. 35 (1), 1–15. http://dx.doi.org/10.1002/cnm.3148.

Hass, H., Jordan, P., Jessberger, H., 1994. Use of artificial ground freezing in three sections of the duesseldorf subway. In: Ground Freezing 94 ISGF.

Hass, H., Schaefers, P., 2006. Application of ground freezing for underground construction in soft ground. In: Geotechnical Aspects of Underground Construction in Soft Ground. Taylor & Francis, London.

Hu, J., Liu, Y., Wei, H., Yao, K., Wang, W., 2017. Finite-element analysis of heat transfer of horizontal ground-freezing method in shield-driven tunneling. Int. J. Geomech. 17, 1–11. http://dx.doi.org/10.1061/(asce)gm.1943-5622.0000978.

Jessberger, H., 1980. Theory and application of ground freezing in civil engineering. Cold Reg. Sci. & Technol. 3, 3–27.

Koopmans, R.W.R., Miller, R., 1966. Soil freezing and soil water characteristic curves 1. Soil Sci. Am. J. 30 (6), 680–685.

Kozlowski, T., 2007. A semi-empirical model for phase composition of water in clay-water systems. Cold Reg. Sci. & Technol. 49, 226–236. http://dx.doi.org/10.1016/j.coldregions.2007.03.013.

Kruschwitz, J., Bluhm, J., 2005. Modeling of ice formation in porous solids with regard to the description of frost damage. Comput. Mater. Sci. 32 (3–4), 407–417.

Kuhl, D., Crisfield, M., 1999. Energy-conserving and decaying algorithms in non-linear structural dynamics. Int. J. Num. Meth. Eng. 45 (5), 569–599.

Lu, J., Pei, W., Zhang, X., Bi, J., Zhao, T., 2019. Evaluation of calculation models for the unfrozen water content of freezing soils. J. Hydrol. 575, 976–985. http://dx.doi.org/10.1016/j.jhydrol.2019.05.031.

Luckner, L., van Genuchten, M., Nielsen, D., 1989. A consistent set of parametric models for the two-phase flow of immiscible fluids in the subsurface. Water Resour. Res. 25 (10), 2187–2193.

Marwan, A., Zhou, M.-M., Zaki, M., Meschke, G., 2016. Optimization of artificial ground freezing in tunneling in the presence of seepage flow. Comput. Geotech. 75, 112–125. http://dx.doi.org/10.1016/j.compgeo.2016.01.004.

McKenzie, J.M., Voss, C.I., Siegel, D.I., 2007. Groundwater flow with energy transport and water-ice phase change: Numerical simulations, benchmarks, and application to freezing in peat bogs. Adv. Water Resour. 30, 966–983. http://dx.doi.org/10.1016/j.advwatres.2006.08.008.

Michalowsld, R.L., 1993. A constitutive model of saturated soils for frost heave simulations. Cold Reg. Sci. & Technol. 22, 47–63.

Mikkola, M., Hartikainen, J., 2002. Computational aspects of soil freezing problem. In: Mang, H., Rammerstorfer, F., Eberhardsteiner, J. (Eds.), Fifth World Congress on Computational Mechanics, Vol. 5. WCCM, Vienna.

Na, S., Sun, W., 2017. Computational thermo-hydro-mechanics for multiphase freezing and thawing porous media in the finite deformation range. Comput. Methods Appl. Mech. Engrg. 318, 667–700. http://dx.doi.org/10.1016/j.cma.2017.01.028, URL https://www.sciencedirect.com/science/article/pii/S0045782516311240.

Nishimura, S., Gens, A., Oliverlla, S., Jardine, R., 2009. THM-coupled finite element analysis of frozen soils: formulation and application. Geotechnique 59 (3), 159–171.

Pérez-Foguet, A., Armero, F., 2002. On the formulation of closest-point projection algorithms in elastoplasticity - part II: Globally convergent schemes. Internat. J. Numer. Methods Engrg. 53, 331–374. http://dx.doi.org/10.1002/nme.279.

Pimentel, E., Papakonstantinou, S., Anagnostou, G., 2012a. Numerical interpretation of temperature distributions from three ground freezing applications in urban tunnelling. Tunnell. Underground Space Technol. 28, 57–69.

Pimentel, E., Sres, A., Anagnostou, G., 2012b. Large-scale laboratory tests on artificial ground freezing under seepage-flow conditions. Geotechnique 62 (3), 227–241.

Saberi, P., Koenig, C., Meschke, G., 2021a. A hysteresis model for the unfrozen liquid content in freezing porous media. Comput. Geotech. 134, 104048. http://dx.doi.org/10.1016/j.compgeo.2021.104048.

Saberi, P.S., König, C., Meschke, G., 2021b. Corrigendum to “a hysteresis model for the unfrozen liquid content in freezing porous media”. Comput. Geotech. 137, 104298. http://dx.doi.org/10.1016/j.compgeo.2021.104298, URL https://www.sciencedirect.com/science/article/pii/S0266352X21002962.

Spaans, E.J., Baker, J.M., 1996. The soil freezing characteristic: Its measurement and similarity to the soil moisture characteristic. Soil Sci. Am. J. 60 (1), 13–19.

Sres, A., 2009. Theoretische und experimentelle Untersuchungen zur Künstlichen Bodenvereisung im Strömenden Grundwasser (Ph.D. thesis). ETH Zürich.

Tian, H., Wei, C., Wei, H., Zhou, J., 2014. Freezing and thawing characteristics of frozen soils: Bound water content and hysteresis phenomenon. Cold Reg. Sci. & Technol. 103, 74–81. http://dx.doi.org/10.1016/j.coldregions.2014.03.007.

Tounsi, H., Rouabhi, A., Tijani, M., Gu?in, F., 2019. Thermo-hydro-mechanical modeling of artificial ground freezing: Application in mining engineering. Rock Mech. Rock Eng. http://dx.doi.org/10.1007/s00603-019-01786-9.

Vitel, M., Rouabhi, A., Tijani, M., Gu?in, F., 2016. Modeling heat and mass transfer during ground freezing subjected to high seepage velocities. Comput. Geotech. 73, 1–15. http://dx.doi.org/10.1016/j.compgeo.2015.11.014, URL https://www.sciencedirect.com/science/article/pii/S0266352X1500244X.

Vu, Q.H., Pereira, J.M., Tang, A.M., 2022. Effect of fines content on soil freezing characteristic curve of sandy soils. Acta Geotech. 17, 4921–4933. http://dx.doi.org/10.1007/s11440-022-01672-9.

Wettlaufer, J.S., Worster, M.G., Wilen, L.A., Dash, J.G., 1996. A theory of premelting dynamics for all power law forces. Appl. Phys. Laboratory Univ. Washington 76.

Williams, P.J., 1964. Unfrozen water content of frozen soils and soil moisture suction. Géotechnique 14 (3), 231–246. http://dx.doi.org/10.1680/geot.1964.14.3.231.

Zhang, M., Pei, W., Li, S., Lu, J., Jin, L., 2017. Experimental and numerical analyses of the thermo-mechanical stability of an embankment with shady and sunny slopes in permafrost regions. Appl. Therm. Eng. 127, 1478–1487. http://dx.doi.org/10.1016/j.applthermaleng.2017.08.074.

Zhou, M.-M., Meschke, G., 2013. A three-phase THM coupled FE model for freezing soils. Int. J. Numer. Anal. Methods Geomech. 37 (18), 3173–3193. http://dx.doi.org/10.1002/nag.2184.

Zhou, Y., Zhou, J., you Shi, X., qing Zhou, G., 2019. Practical models describing hysteresis behavior of unfrozen water in frozen soil based on similarity analysis. Cold Reg. Sci. & Technol. 157, 215–223. http://dx.doi.org/10.1016/j.coldregions.2018.11.002.